

## Critical Dependence of Molecular Weight on Thermoresponsive Behavior of Diblock Copolymer Worm Gels in Aqueous Solution

Nicholas J. Warren,<sup>\*,†,‡</sup> Matthew J. Derry,<sup>†</sup> Oleksandr O. Mykhaylyk,<sup>†</sup> Joseph R. Lovett,<sup>†</sup> Liam P. D. Ratcliffe,<sup>†</sup> Vincent Ladmiral,<sup>||</sup> Adam Blanazs,<sup>§</sup> Lee A. Fielding,<sup>⊥</sup> and Steven P. Armes<sup>\*,†,‡</sup>

<sup>†</sup>Department of Chemistry, University of Sheffield, Brook Hill, Sheffield S3 7HF, U.K.

<sup>‡</sup>School of Chemical and Process Engineering, University of Leeds, Leeds LS2 9JT, U.K.


<sup>§</sup>BASF SE, GMV/P-B001, 67056 Ludwigshafen, Germany

<sup>||</sup>Ingénierie et Architectures Macromoléculaires, CNRS, UM, ENSCM, Institut Charles Gerhardt UMR 5253, Place Eugène Bataillon, Cedex 5 34095 Montpellier, France

<sup>⊥</sup>School of Materials, University of Manchester, Oxford Road, Manchester M13 9PL, U.K.

### Supporting Information

**ABSTRACT:** Reversible addition–fragmentation chain transfer (RAFT) aqueous dispersion polymerization of 2-hydroxypropyl methacrylate was used to prepare three poly(glycerol monomethacrylate)<sub>x</sub>–poly(2-hydroxypropyl methacrylate)<sub>y</sub> (denoted G<sub>x</sub>-H<sub>y</sub> or PGMA-PPHMA) diblock copolymers, namely G<sub>37</sub>-H<sub>80</sub>, G<sub>54</sub>-H<sub>140</sub>, and G<sub>71</sub>-H<sub>200</sub>. A master phase diagram was used to select each copolymer composition to ensure that a pure worm phase was obtained in each case, as confirmed by transmission electron microscopy (TEM) and small-angle x-ray scattering (SAXS) studies. The latter technique indicated a mean worm cross-sectional diameter (or worm width) ranging from 11 to 20 nm as the mean degree of polymerization (DP) of the hydrophobic PPHMA block was increased from 80 to 200. These copolymer worms form soft hydrogels at 20 °C that undergo degelation on cooling. This thermo-responsive behavior was examined using variable temperature DLS, oscillatory rheology, and SAXS. A 10% w/w G<sub>37</sub>-H<sub>80</sub> worm dispersion dissociated to afford an aqueous solution of molecularly dissolved copolymer chains at 2 °C; on returning to ambient temperature, these chains aggregated to form first spheres and then worms, with the original gel strength being recovered. In contrast, the G<sub>54</sub>-H<sub>140</sub> and G<sub>71</sub>-H<sub>200</sub> worms each only formed spheres on cooling to 2 °C, with thermoreversible (de)gelation being observed in the former case. The sphere-to-worm transition for G<sub>54</sub>-H<sub>140</sub> was monitored by variable temperature SAXS: these experiments indicated the gradual formation of longer worms at higher temperature, with a concomitant reduction in the number of spheres, suggesting worm growth via multiple 1D sphere–sphere fusion events. DLS studies indicated that a 0.1% w/w aqueous dispersion of G<sub>71</sub>-H<sub>200</sub> worms underwent an irreversible worm-to-sphere transition on cooling to 2 °C. Furthermore, irreversible degelation over the time scale of the experiment was also observed during rheological studies of a 10% w/w G<sub>71</sub>-H<sub>200</sub> worm dispersion. Shear-induced polarized light imaging (SIPLI) studies revealed qualitatively different thermoreversible behavior for these three copolymer worm dispersions, although worm alignment was observed at a shear rate of 10 s<sup>-1</sup> in each case. Subsequently conducting this technique at a lower shear rate of 1 s<sup>-1</sup> combined with ultra small-angle x-ray scattering (USAXS) also indicated that worm branching occurred at a certain critical temperature since an upturn in viscosity, distortion in the birefringence, and a characteristic feature in the USAXS pattern were observed. Finally, SIPLI studies indicated that the characteristic relaxation times required for loss of worm alignment after cessation of shear depended markedly on the copolymer molecular weight.



### INTRODUCTION

The self-assembly of AB diblock copolymers in a solvent that is selective for one of the two blocks has been known for more than 50 years.<sup>1,2</sup> A wide range of copolymer morphologies can be prepared in dilute solution using various postpolymerization processing strategies, such as solvent exchange,<sup>3</sup> pH switch,<sup>4,5</sup> or thin film rehydration.<sup>6</sup> In principle, the copolymer morphology depends on the relative volume fractions of the solvophilic and solvophobic blocks according to the packing parameter,  $P$  as introduced by Israelachvili and co-workers for surfactant self-assembly in 1976.<sup>7</sup> Highly anisotropic diblock

copolymer nanoparticles variously described in the literature as rods,<sup>8–12</sup> cylinders,<sup>13,14</sup> filomicelles,<sup>15–19</sup> or worms<sup>8,9,20–23</sup> (the latter term is preferred in this study) can be produced, but typically only within a relatively narrow  $P$  range (e.g.,  $0.33 < P \leq 0.50$ ) compared to either spheres ( $P \leq 0.33$ ) or vesicles ( $0.50 < P \leq 1.00$ ). It is also well-known that self-assembly of

Received: August 1, 2018

Revised: October 2, 2018

Published: October 16, 2018

surfactants,<sup>24</sup> oligopeptides,<sup>25–27</sup> or block copolymers<sup>8,21,28–36</sup> can produce free-standing gels in various solvents.

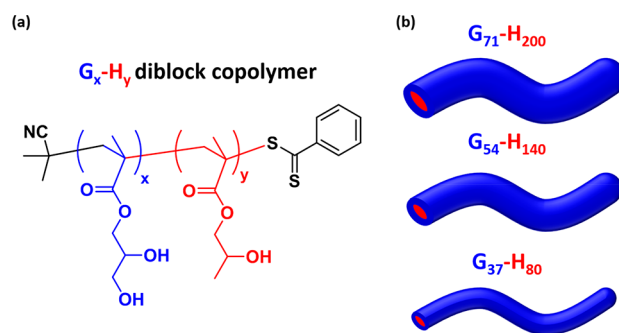
Polymerization-induced self-assembly (PISA) has recently become established as a highly versatile method for the direct preparation of a wide range of diblock copolymer nano-objects in the form of *concentrated* dispersions (up to 50% solids).<sup>37–40</sup> Briefly, PISA involves growing a second block from a soluble precursor block under conditions whereby the second block gradually becomes insoluble, hence driving *in situ* self-assembly to form sterically stabilized nanoparticles. In particular, such formulations enable the convenient and reproducible synthesis of a wide range of diblock copolymer worms in various solvents<sup>28,32,41–43</sup> such as water,<sup>8,16,21,32,44–46</sup> various alcohols,<sup>47–50</sup> or *n*-alkanes.<sup>28,51,52</sup> In each case, free-standing gels can be obtained above a certain critical copolymer concentration known as the critical gelation concentration (CGT).<sup>53</sup> Moreover, such worm gels can exhibit interesting thermoresponsive behavior: adjusting the solution temperature leads to a worm-to-sphere transition, which leads to *in situ* degelation.<sup>8,21,28,32,47</sup> For example, poly(glycerol monomethacrylate)–poly(2-hydroxypropyl methacrylate) (PGMA–PHPMA) diblock copolymer worm gels undergo degelation on cooling from 20 to 5 °C.<sup>21</sup> This morphological transition is reversible at a sufficiently high copolymer concentration, with worm gels being re-formed on returning to 20 °C. Complementary behavior has been observed for nonaqueous worm gels, whereby heating is required to induce a worm-to-sphere transition.<sup>28,47</sup> In both cases these observations can be rationalized in terms of surface plasticization of the worm cores.<sup>8,21,28,47</sup> Verber et al.<sup>21</sup> characterized a series of PGMA<sub>x</sub>–PHPMA<sub>y</sub> (herein denoted G<sub>x</sub>–H<sub>y</sub>) worm gels where the mean degree of polymerization (DP or *x*) of the PGMA block was fixed at 54 and that of the PHPMA block (*y*) was varied between 90 and 220. Spherical nanoparticles were formed when targeting *y* = 90, whereas linear worms were obtained for 130 ≤ *y* < 140, branched worms produced at *y* = 145, and worm clusters observed at higher DPs (with vesicles eventually being formed at *y* = 170). Targeting higher DPs for the core-forming PHPMA block also led to an increase in the gel storage modulus (*G'*). Following this initial study, this prototypical diblock copolymer formulation was subsequently modified to tune the gel modulus<sup>54,55</sup> and also the CGT.<sup>40,56</sup>

In principle, the reversible nature of the thermally induced worm-to-sphere transition can be exploited for facile sterilization via cold ultrafiltration: cold free-flowing spherical nanoparticles (30–40 nm diameter) easily pass through 0.45 μm pores, whereas the much larger (>500 nm) bacteria are removed, with a sterile worm gel being re-formed on returning to 20 °C.<sup>8</sup> Furthermore, these thermoresponsive worm gels can be readily reconstituted from freeze-dried copolymer powder in either pure water, phosphate buffered saline, or various cell culture media.<sup>57,58</sup> Given that these worm gels are highly biocompatible, potential biological applications include a convenient 3D matrix for the proliferation of conventional cell lines,<sup>55</sup> a unique storage medium that induces stasis in human stem cells,<sup>58</sup> and a potential new approach for the cryopreservation of red blood cells.<sup>59</sup> Moreover, the gel modulus of G<sub>x</sub>–H<sub>y</sub> worm gels can be significantly increased by incorporating disulfide bonds into the hydrophilic PGMA stabilizer block.<sup>54,55,60</sup>

In this study, we revisit our “first generation” G<sub>x</sub>–H<sub>y</sub> worm gel formulation to examine its properties in more detail. More specifically, we systematically adjust the mean DPs of the

PGMA and PHPMA blocks to generate three worm gels of varying worm cross-sectional diameter (hereafter denoted the worm thickness; see Scheme 1). We utilize a combination of

**Scheme 1.** (a) Chemical Structure of Poly(glycerol monomethacrylate)–Poly(2-hydroxypropyl methacrylate) Diblock Copolymer (G<sub>x</sub>–H<sub>y</sub>; Where *x* = 37, 54, and 71 and *y* = 80, 140, and 200); (b) Schematic Representation of the Increase in Cross-Sectional Worm Radius When Increasing the Mean Degree of Polymerization of the Corona PGMA and the Core-Forming PHPMA Block



dynamic light scattering (DLS), oscillatory rheology, and small-angle X-ray scattering (SAXS) to demonstrate remarkably diverse behavior for such worm dispersions. We also conduct variable temperature shear-induced polarized light imaging (SIPLI) experiments.<sup>61,62</sup> This rheo-optical technique has been used to identify the onset of shear-induced crystallization in both synthetic polymers<sup>62</sup> and silk<sup>63</sup> and also to study the structural orientation in block copolymer solutions<sup>62</sup> and liquid crystals.<sup>60</sup> More recently, SIPLI has been used to demonstrate that G<sub>x</sub>–H<sub>y</sub> worms can be aligned under shear and also to obtain characteristic worm relaxation times after cessation of shear.<sup>61</sup>

## EXPERIMENTAL SECTION

**Materials.** Glycerol monomethacrylate (GMA; 99.8%) and 2-hydroxypropyl methacrylate (HPMA) were kindly donated by GEO Specialty Chemicals (Hythe, UK). The latter monomer was extensively purified by distillation to remove its dimethacrylate impurity, which can otherwise result in significant branching and/or cross-linking.<sup>64</sup> 2-Cyano-2-propyl dithiobenzoate (CPDB, 75% purity as judged by <sup>1</sup>H NMR spectroscopy) was purchased from Strem Chemicals (Cambridge, UK). 4,4'-Azobis(4-cyanopentanoic acid) (ACVA; V-501; 99%) and anhydrous ethanol (99%) were purchased from Sigma-Aldrich (Dorset, UK). All other solvents were of HPLC quality and purchased from Fisher Scientific (Loughborough, UK). Deionized water was used in all experiments. CD<sub>3</sub>OD (99.8%) was purchased from Goss Scientific (Nantwich, UK) and used as received.

### Synthesis of Poly(glycerol monomethacrylate) Using CPDB.

The RAFT solution polymerization of GMA was conducted in ethanol at 70 °C. This protocol afforded PGMA macromolecular chain transfer agents (macro-CTAs; denoted G<sub>x</sub>) with narrow molecular weight distributions in high yield with mean DPs of 37, 54, or 71 detected by <sup>1</sup>H NMR and dimethylformamide (DMF) gel permeation chromatography (GPC) (Table S1). A typical protocol for such syntheses is as follows. For a target composition of PGMA<sub>54</sub> (G<sub>54</sub>), GMA monomer (110.9 g, 0.692 mol) and CPDB RAFT agent (3.015 g, 11.0 mmol; target conversion = 80% and target DP = 50) were weighed into a 500 mL round-bottomed flask and purged with N<sub>2</sub> for 30 min. ACVA initiator (0.570 g, 2.03 mmol; CPDB/ACVA molar ratio = 5.0) and anhydrous ethanol (78.0 g; previously purged with N<sub>2</sub> for 30 min) were then added, and the resulting red solution was degassed for a further 10 min while stirring to form a

homogeneous solution. The flask was subsequently sealed and immersed in an oil bath set at 70 °C. After 120 min, the GMA polymerization was quenched by exposing the reaction solution to air, immersing the reaction flask in liquid nitrogen for 30 s, and finally dilution with methanol (100 mL). A final GMA conversion of 85% was determined by <sup>1</sup>H NMR analysis. The methanolic solution was precipitated twice into a 10-fold excess of dichloromethane. After filtering and washing with dichloromethane, the crude homopolymer was dissolved in water, and residual dichloromethane was evaporated under vacuum. The resulting aqueous solution was freeze-dried to yield ~85 g of product in the form of a pink powder. <sup>1</sup>H NMR analysis indicated a mean DP of 54 for this PGMA macro-CTA. DMF GPC analysis indicated an  $M_n$  of 14200 g mol<sup>-1</sup> and an  $M_w/M_n$  of 1.16 [vs poly(methyl methacrylate) calibration standards].

**Preparation of Worm Gels via RAFT Aqueous Dispersion Polymerization of HPMA.** A typical protocol for the synthesis of a G<sub>x</sub>-H<sub>y</sub> worm gel (for example, a G<sub>54</sub>-H<sub>140</sub> composition) is as follows. G<sub>54</sub> macro-CTA (3.60 g, 0.395 mmol) and HPMA monomer (8.0 g, 55.49 mmol; target DP = 140) were weighed into a 100 mL round-bottomed flask and purged with N<sub>2</sub> for 20 min. ACVA was added (28.3 mg, 0.101 mmol, CTA/ACVA molar ratio = 5.0) and purged with N<sub>2</sub> for a further 5 min. Deionized water (46.1 mL, producing a 20.0% w/w aqueous solution), which had been previously purged with N<sub>2</sub> for 30 min, was then added, and the solution was purged for a further 5 min prior to immersion in an oil bath set at 70 °C. The reaction solution was stirred for 3 h before the HPMA polymerization was quenched by exposure to air. The absence of signals owing to the vinyl protons of the HPMA monomer in the <sup>1</sup>H NMR spectrum indicated that the polymerization had attained more than 99% conversion. The resulting dispersion formed a pink free-standing gel.

**NMR Spectroscopy.** <sup>1</sup>H NMR spectra were recorded using a 400 MHz Bruker Avance-400 spectrometer with 64 scans being averaged per spectrum.

**Gel Permeation Chromatography.** 0.50% w/w copolymer solutions were prepared in DMF containing DMSO (10 μL mL<sup>-1</sup>) as a flow-rate marker. GPC measurements were conducted using HPLC-grade DMF eluent containing 10 mM LiBr at 60 °C at a flow rate of 1.0 mL min<sup>-1</sup>. An Agilent Technologies 1260 Infinity GPC/SEC system fitted with two Polymer Laboratories PL gel 5 μm Mixed-C columns connected in series, and a refractive index detector was used to assess molecular weight distributions. Sixteen near-monodisperse poly(methyl methacrylate) standards ranging from  $M_p = 645$  to 2480000 g mol<sup>-1</sup> were used for calibration.

**Dynamic Light Scattering (DLS).** Variable temperature DLS studies were conducted on 0.1% w/w aqueous copolymer dispersions using a Malvern Zetasizer Nano ZS instrument. Measurements were conducted from 40 to 2 °C in 1 °C increments, with an equilibration time of 2 min being allowed at each temperature. Intensity-average hydrodynamic diameters were calculated using the Stokes–Einstein equation and a non-negative least-squares (NNLS) algorithm. All data were averaged over three consecutive runs comprising ten measurements each. For highly anisotropic wormlike particles, it is emphasized that DLS reports a “sphere-equivalent” diameter that corresponds to neither the mean worm length nor the mean worm width. Nevertheless, DLS can be used to monitor the relative changes in particle size that may occur during thermal cycles as a result of a worm-to-sphere transition.

**Transmission Electron Microscopy (TEM).** Diblock copolymer dispersions were diluted 50-fold to 0.20% w/w at 20 °C (for G<sub>54</sub>-H<sub>140</sub> and G<sub>71</sub>-H<sub>200</sub>) or 50 °C (for G<sub>37</sub>-H<sub>80</sub>) prior to staining. Copper/palladium TEM grids (Agar Scientific, UK) were surface-coated in-house to yield a thin film of amorphous carbon. The grids were then treated with a plasma glow discharge for 45 s to create a hydrophilic surface. One 12 μL droplet of each aqueous copolymer dispersion was then placed onto a freshly treated grid for 30 s and then blotted with filter paper to remove excess solution. To stain the deposited nanoparticles, a 0.75% w/w aqueous solution of uranyl formate (9 μL) was placed via micropipet on the sample-loaded grid for 20 s and then carefully blotted to remove excess stain. Each grid was then carefully dried using a vacuum hose. Imaging was performed using a

FEI Tecnai Spirit TEM instrument equipped with a Gatan 1kMS600CW CCD camera and operating at 80 kV.

**Rheology Measurements.** An AR-G2 rheometer equipped with a variable temperature Peltier plate and a 40 mm 2° aluminum cone was used for all experiments. An oscillatory mode was used to measure viscosity, loss modulus ( $G''$ ), and storage modulus ( $G'$ ) as a function of percentage strain amplitude, angular frequency, and temperature to assess critical gelation temperatures, gel strengths, and gel viscosities. Percentage strain amplitude sweeps between 0.1 and 500 rad s<sup>-1</sup> were conducted at constant temperatures where worms were the dominant morphology (40 °C for G<sub>37</sub>-H<sub>80</sub> and 25 °C for G<sub>54</sub>-H<sub>140</sub> and G<sub>71</sub>-H<sub>200</sub>) using angular frequencies of either 1 or 10 rad s<sup>-1</sup>. Angular frequency sweeps were conducted at the same temperatures as the strain sweeps using an applied strain amplitude of 1.0%. Temperature sweeps were conducted using the same applied strain amplitude and at angular frequencies of either 1 or 10 rad s<sup>-1</sup>. Measurements were recorded at 1 °C intervals, allowing 3 min for thermal equilibration in each case.

**SAXS Measurements.** Small-angle X-ray scattering patterns were recorded using three X-ray radiation sources: Diamond Light Source synchrotron (Didcot, UK), station I22 ( $\lambda = 0.1001$  nm, camera length = 10.0 m and Dectris Pilatus 2 M pixel detector), European Synchrotron Radiation Facilities (ESRF, Grenoble, France), station ID02 ( $\lambda = 0.1$  nm, camera length = 3.0 m and Rayonix MX-170HS CCD detector), and a laboratory SAXS instrument (Xeuss 2.0, Xenocs, France) equipped with a liquid gallium MetalJet X-ray source (Excillum, Sweden) ( $\lambda = 0.134$  nm, camera length = 3.8 m, and Dectris Pilatus 1M pixel detector). The latter was used for concentration-dependent measurements. In such experiments the scattering vector  $q$  is given by  $q = \frac{4\pi \sin \theta}{\lambda}$ , where  $\theta$  is a half of the scattering angle. 2.0 mm glass capillaries were used as sample holders and where required, the temperature was controlled using a heating/cooling capillary stage (Linkam Scientific Instruments Ltd., Tadworth, UK). SAXS measurements were conducted after dilution of each as-synthesized 20% w/w copolymer dispersion to the desired concentration using deionized water. 2D scattering data obtained at synchrotron sources were reduced to 1D patterns using standard beamline data-handling protocols, whereas data collected by the Xenocs Xeuss 2.0 instrument were reduced using the Foxtrot software package developed at SOLEIL synchrotron. All such data were further reduced (i.e., normalized and background-subtracted) and then fitted by a structural model using Irena SAS macros for Igor Pro.<sup>65</sup>

Structural data were determined by fitting 1D SAXS patterns to an appropriate model for spheres and/or worms (see the [Supporting Information](#) for the model description). In particular, this approach enabled calculation of the mean worm core radius, ( $R_{cw}$ ), sphere core radius, ( $R_{cs}$ ), the radius of gyration of the PGMA stabilizer chains ( $R_g$ ), the mean water content within the PHPMA cores ( $x_{sol}$ ), the worm contour length ( $L_c$ ), and the worm Kuhn length ( $L_k$ ).

**Shear-Induced Polarized Light Imaging.** A mechano-optical rheometer (Anton Paar Physica MCR301 equipped with a SIPLI attachment) was used for the time-resolved shear alignment experiments. This recently commercialized instrument has been described in detail elsewhere.<sup>61</sup> The measurements were performed using a plate–plate geometry composed of a 25 mm polished steel top plate and a fused quartz bottom plate coupled with a variable temperature Peltier system. The gap between plates  $d_{gap}$  was set at 1.0 mm for all experiments. An additional Peltier hood was used to achieve precise control of the sample temperature. An Edmund Optics 150 W MI-150 high-intensity fiber-optic white light source was used for sample illumination. The polarizer and analyzer axes were crossed at 90° to obtain polarized light images (PLIs), which were recorded using a color CCD camera (Lumenera Lu165c). The dispersion effective viscosity was measured simultaneously by the mechanical rheometer as a function of temperature at a heating/cooling rate of 1.0 °C min<sup>-1</sup> at a constant angular speed of 0.8 rad s<sup>-1</sup>. For worm relaxation studies, dispersions were subjected to this angular speed for 60 s at various temperatures, prior to cessation of shear. Images were captured at 250 ms intervals until the birefringence was no longer

visible (i.e., complete disappearance of the characteristic Maltese cross pattern). The resulting polarized light images were stacked and then sliced by a plane forming an angle of 45° with polarizer and analyzer axes and perpendicular to the imaging plane<sup>60</sup> using ImageJ software. The obtained 2D image was subsequently converted to grayscale and exported as a text file containing the relative intensities of each pixel. The intensity along the line of the 2D image corresponding to a shear rate,  $\dot{\gamma}$  of 5 s<sup>-1</sup> was plotted vs time, giving an exponential decay curve, from which a characteristic relaxation time,  $\tau_1$ , can be extracted and thus the relaxation half-life,  $\tau_{1/2}$ , calculated, where  $\tau_{1/2} = \tau_1 \ln(2)$ .

## RESULTS AND DISCUSSION

Initially, three PGMA macro-CTAs were prepared via RAFT solution polymerization at 70 °C in ethanol by varying the monomer/CTA molar ratio to adjust the target DP. <sup>1</sup>H NMR studies of these purified macro-CTAs indicated mean DPs of 37, 54, and 71 (by comparing the integrated aromatic dithiobenzoate signals between 7.36 and 7.94 ppm to those corresponding to the combined signals assigned to the protons associated with the pendent GMA repeat units between 3.40 and 4.29 ppm).  $M_n$  values of 10600, 14200, and 17400 g mol<sup>-1</sup> were obtained from DMF GPC analysis (see Figure S1), which confirmed the expected systematic increase in  $M_n$  for these three macro-CTAs (Table S1).

To determine the appropriate mean PHPMA DP required to target the worm morphology for each of the three PGMA stabilizer blocks, a suitable phase diagram was constructed based on the copolymer morphologies previously assigned via *post-mortem* TEM analyses for this PISA formulation (Figure 1).<sup>21,43,57,66</sup> This phase diagram was used to predict specific

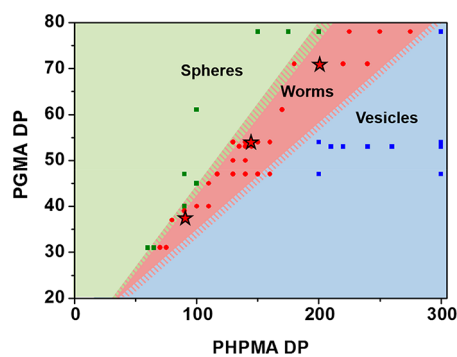


Figure 1. Phase diagram constructed for  $G_x-H_y$  diblock copolymer nano-objects to determine the precise copolymer composition for the pure worm phase. Each point represents the copolymer morphology assigned on the basis of *post-mortem* TEM studies. Green squares indicate spheres, red circles indicate worms, and blue squares indicate vesicles. Shaded boundaries represent regions of uncertainty. The three stars indicate the specific copolymer compositions used in this study. All copolymer syntheses were conducted at 20% w/w solids except for those involving PGMA DPs below 47, which were conducted at 10% w/w solids. These can be included in this phase diagram because the copolymer morphologies produced using such short stabilizer blocks exhibit no concentration dependence.

diblock copolymer compositions for PISA syntheses conducted at 20% w/w solids that corresponded to a pure worm morphology in each case (e.g.,  $G_{37}-H_{80}$ ,  $G_{54}-H_{140}$ , and  $G_{71}-H_{200}$ ). It has to be noted that some PISA syntheses were conducted at 10% w/w solids, but in such cases the PGMA stabilizer block was sufficiently short that the copolymer morphology was essentially concentration-independent;<sup>43</sup> thus, such data could be legitimately included in the phase diagram

(Figure 1). <sup>1</sup>H NMR studies confirmed that each polymerization proceeded to more than 99% HPMA conversion based on the disappearance of vinyl proton signals initially observed at 5.5 and 6.2 ppm (Figure S2). DMF GPC studies confirmed a systematic increase in  $M_n$  with target DP (Figure 2), while  $M_w/M_n$  values remained below 1.15 in all cases.

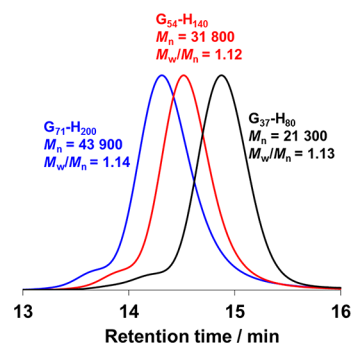
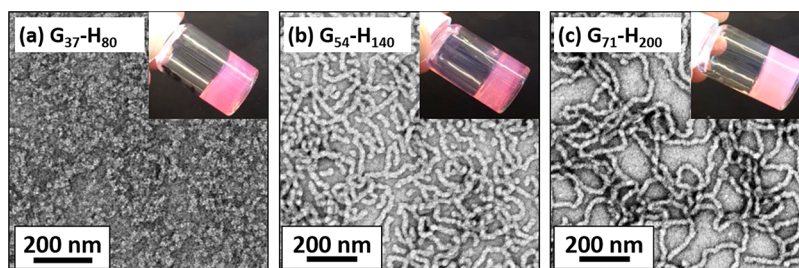


Figure 2. DMF gel permeation chromatograms recorded for the three diblock copolymers used in this work:  $G_{37}-H_{80}$ ,  $G_{54}-H_{140}$ , and  $G_{71}-H_{200}$ .  $M_n$  and  $M_w/M_n$  values were calculated relative to a series of 16 near-monodisperse poly(methyl methacrylate) calibration standards.

TEM studies (Figure 3) conducted on each of these dried copolymer dispersions confirmed the presence of diblock copolymer worms for  $G_{54}-H_{140}$  and  $G_{71}-H_{200}$ . However, the TEM image obtained for the  $G_{37}-H_{80}$  dispersion was inconclusive, despite tube inversion experiments indicating the formation of a free-standing gel (Figure 3a, inset). It has to be noted that TEM studies are performed at relatively low copolymer concentrations (0.20 w/w %) which could cause morphological transformation of the self-assembled copolymer nano-objects upon dilution from concentrated dispersions.

In this respect SAXS is a more reliable technique which enables analysis of copolymer dispersions at high concentrations to be performed. Accordingly, SAXS studies have confirmed a wormlike morphology in all three cases (Figure 4). More specifically, each SAXS pattern clearly exhibited a gradient close to  $-1$  in the low  $q$  region, as expected for highly anisotropic rods/cylinders/worms; similar findings have been recently reported for various types of diblock copolymer worms prepared using PISA.<sup>28,40,67</sup> Furthermore, the intensity minimum observed at higher  $q$  associated with the worm cross-sectional radius for  $G_{37}-H_{80}$ ,  $G_{54}-H_{140}$ , and  $G_{71}-H_{200}$  lies at approximately 0.55, 0.4, and 0.3 nm<sup>-1</sup>, respectively, indicating an increase in the cross-sectional radius with higher copolymer molecular weight. Fitting each SAXS pattern using a wormlike micelle model enabled extraction of several parameters (Figure 5):  $R_{cw}$  values for the  $G_{37}-H_{80}$ ,  $G_{54}-H_{140}$ , and  $G_{71}-H_{200}$  worms were determined to be 5.6, 8.4, and 10.8 nm, respectively (Table 1).

Similarly, the radius of gyration ( $R_g$ ) for the  $G_{37}$ ,  $G_{54}$ , and  $G_{71}$  stabilizer blocks was determined to be 1.4, 1.9, and 2.4 nm, respectively. These radii are physically reasonable compared to the calculated theoretical values of 1.6, 1.9, and 2.2 nm (see the Supporting Information for further details).  $R_{cw}$  and  $R_g$  were subsequently used to calculate the overall worm cross-sectional diameter,  $d_w$ , where  $d_w = 4R_g + 2R_{cw}$ . These diameters were determined to be 16.8, 24.4, and 31.2 nm for  $G_{37}-H_{80}$ ,  $G_{54}-H_{140}$ , and  $G_{71}-H_{200}$ , respectively (Table 1). Sugihara et al.<sup>42</sup> estimated worm cross-sectional diameters ranging from 22 to 41 nm for PMPC<sub>25</sub>-PHPMA<sub>x</sub> worms, when  $x$  was varied



**Figure 3.** TEM images obtained for (a)  $G_{37}\text{-}H_{80}$ , where no discernible copolymer morphologies were observed owing to molecular dissolution on dilution, (b)  $G_{54}\text{-}H_{140}$  copolymer worm, and (c)  $G_{71}\text{-}H_{200}$  copolymer worms. Each copolymer dispersion was diluted from 20% to 0.20% w/w using water (pH 6) at 20 °C. Inset digital images were recorded for 20% w/w dispersions.

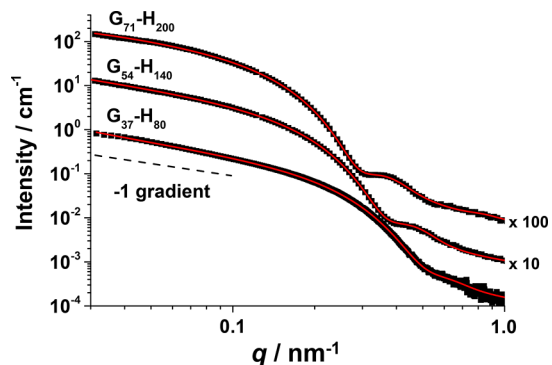


**Figure 4.** Small-angle X-ray scattering (SAXS) patterns for aqueous dispersions of  $G_{37}\text{-}H_{80}$  (1.0% w/w),  $G_{54}\text{-}H_{140}$  (1.0% w/w), and  $G_{71}\text{-}H_{200}$  (1.0% w/w) diblock copolymer worms.  $G_{54}\text{-}H_{140}$  and  $G_{71}\text{-}H_{200}$  were recorded at 25 °C, whereas  $G_{37}\text{-}H_{80}$  was recorded at 35 °C to ensure that its original worm morphology was retained on dilution. The red solid curves are calculated fits to the data using a wormlike micelle model (see the Supporting Information). A gradient of  $-1$  is indicated as guidance for the eye. Each SAXS pattern is offset by an arbitrary multiplication factor to avoid overlap of the data. The fitting results are presented in Table 1.

between 220 and 400. The diameter obtained for the  $G_x\text{-}H_y$  worms is significantly smaller, which most likely reflects the use of TEM to characterize PMPC-PPMA worms compared to SAXS characterization of the  $G_x\text{-}H_y$  worms in this study. In this context, it is important to recognize that imaging techniques such as TEM and atomic force microscopy (AFM) are used to analyze dehydrated worms prepared by drying dilute dispersions, whereas SAXS measurements are conducted on aqueous worm dispersions. The latter technique is much more statistically robust because X-ray scattering data are averaged over millions of worms. In contrast, far fewer worms are typically analyzed using TEM or AFM. For example, inspection of the TEM images shown in Figures 3b and 3c suggests approximate worm cross-sectional diameters of  $20 \pm 5$  and  $24 \pm 7$  nm (averaged over 50 measurements in each case) for  $G_{54}\text{-}H_{140}$  and  $G_{71}\text{-}H_{200}$  worms, respectively. Furthermore, it is not clear whether the TEM measurements include both the worm cores and (part of) the worm coronas or are restricted to just the worm cores.

The worm cross-sectional radius,  $R_{cw}$ , determined by SAXS analysis of the three  $G_x\text{-}H_y$  worms described herein can be fitted to a power law such that  $2R_{cw} = kN^\alpha$  (where  $k$  is a constant that depends on the Flory–Huggins parameter,  $N$  is the DP of the PHPMA block, and  $\alpha$  is an exponent that depends on the extent of chain stretching within the worm cores). An  $\alpha$  exponent of 0.70 is obtained from this power law

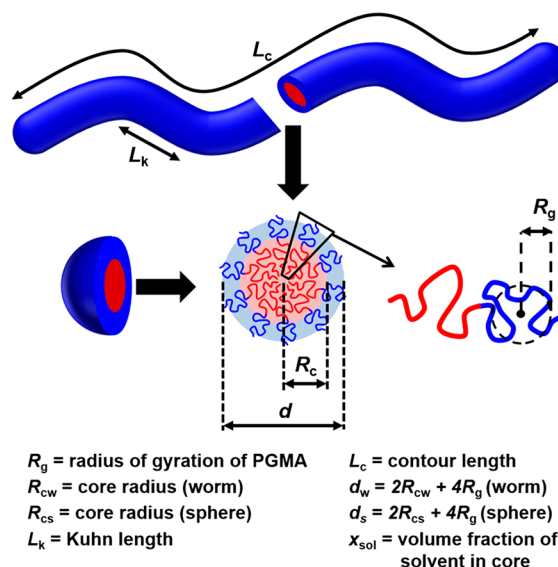


**Figure 5.** Schematic representation of the various structural parameters obtained by fitting a wormlike micelle and/or a spherical micelle model to experimental SAXS data.  $R_c$  corresponds to  $R_{cs}$  when considering the sphere core radius and  $R_{cw}$  when considering the worm core cross-sectional radius. Similarly,  $d$  corresponds to  $d_s$  when considering the sphere core radius and  $d_w$  when considering the worm core cross-sectional diameter.

fit (data not shown), indicating that the core-forming PHPMA chains are intermediate between their fully stretched and unperturbed states.

The volume fraction of water within the worm cores,  $x_{sol}$ , remains relatively low (0.02) for both  $G_{54}\text{-}H_{140}$  and  $G_{71}\text{-}H_{200}$  at 25 °C but increases up to 0.14 for  $G_{37}\text{-}H_{80}$  (Table 1). This agrees with observations made during variable temperature  $^1\text{H}$  NMR studies; the pendent methyl signal at 1.4 ppm assigned to the HPMA repeat units is more prominent for  $G_{37}\text{-}H_{80}$  than for the other two copolymers, indicating that the former is more plasticized (Figures S3–S5). This is also consistent with the apparent partial dissociation of such  $G_{37}\text{-}H_{80}$  worms on dilution prior to TEM studies (Figure 3a). Unfortunately, overlapping  $^1\text{H}$  NMR signals in this spectral region prevents more quantitative analysis.

The worm contour length,  $L_c$ , and Kuhn length,  $L_k$ , can also be determined by fitting the SAXS data. However, the limited  $q$  range accessed in our SAXS experiments means that these parameters are not particularly reliable. Nevertheless, the SAXS model has indicated that  $L_c$  exceeds 800 nm for all three types of worms, with larger  $L_c$  values being observed with increasing copolymer molecular weight. These results are in a reasonable

**Table 1.** Summary of Copolymer Molecular Weight Data (Number-Average Molecular Weight,  $M_n$ , and Dispersity,  $M_w/M_n$ ) Obtained from DMF GPC (Using Refractive Index Detection vs a Series of Near-Monodisperse PMMA Standards) and Various Structural Parameters Obtained from Fitting SAXS Patterns Recorded for 1.0% w/w Aqueous Dispersions of  $G_x$ - $H_y$  Diblock Copolymer Worms<sup>a</sup>

composition	GPC		SAXS					
	$M_n$	$M_w/M_n$	$R_{cw}$ (nm)	$R_g$ (nm)	$d_w$ (nm)	$x_{sol}$	$L_k$ (nm)	$L_c$ (nm)
$G_{37}$ - $H_{80}$	21300	1.13	5.6	1.4	16.8	0.14	192	866
$G_{54}$ - $H_{140}$	31800	1.12	8.4	1.9	24.4	0.02	246	970
$G_{71}$ - $H_{200}$	43900	1.14	10.8	2.4	31.2	0.02	570	>1500

<sup>a</sup> $G_{54}$ - $H_{140}$  and  $G_{71}$ - $H_{200}$  were recorded at 25 °C, whereas  $G_{37}$ - $H_{80}$  was recorded at 35 °C to ensure that its original worm morphology was retained on dilution [mean worm core radius ( $R_{cw}$ ), radius of gyration of the  $G_x$  stabilizer chains ( $R_g$ ), total worm cross section ( $d_w = 2R_{cw} + 4R_g$ ), worm contour length ( $L_c$ ), worm Kuhn length ( $L_k$ ), and solvent fraction in the worm cores ( $x_{sol}$ )].

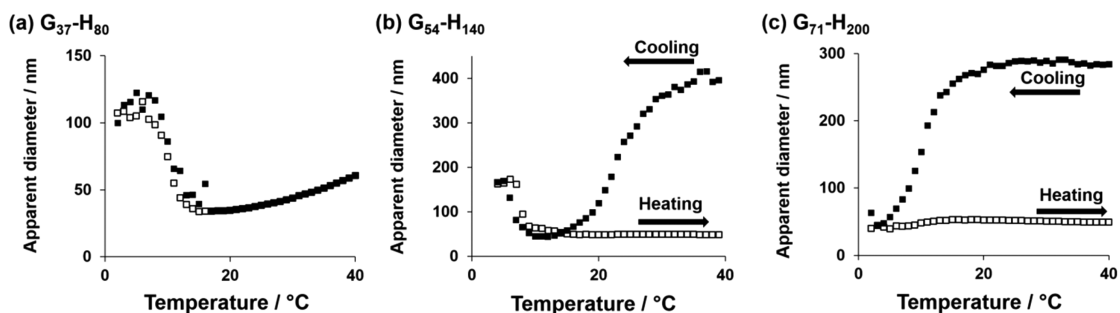


**Figure 6.** Variable-temperature dynamic light scattering studies showing the sphere-equivalent diameter determined during thermal cycles conducted on 0.1% w/w dilute aqueous dispersions of (a)  $G_{37}$ - $H_{80}$ , (b)  $G_{54}$ - $H_{140}$ , and (c)  $G_{71}$ - $H_{200}$  worms. Filled symbols indicate the (first) cooling cycle, whereas hollow symbols indicate the heating cycle.

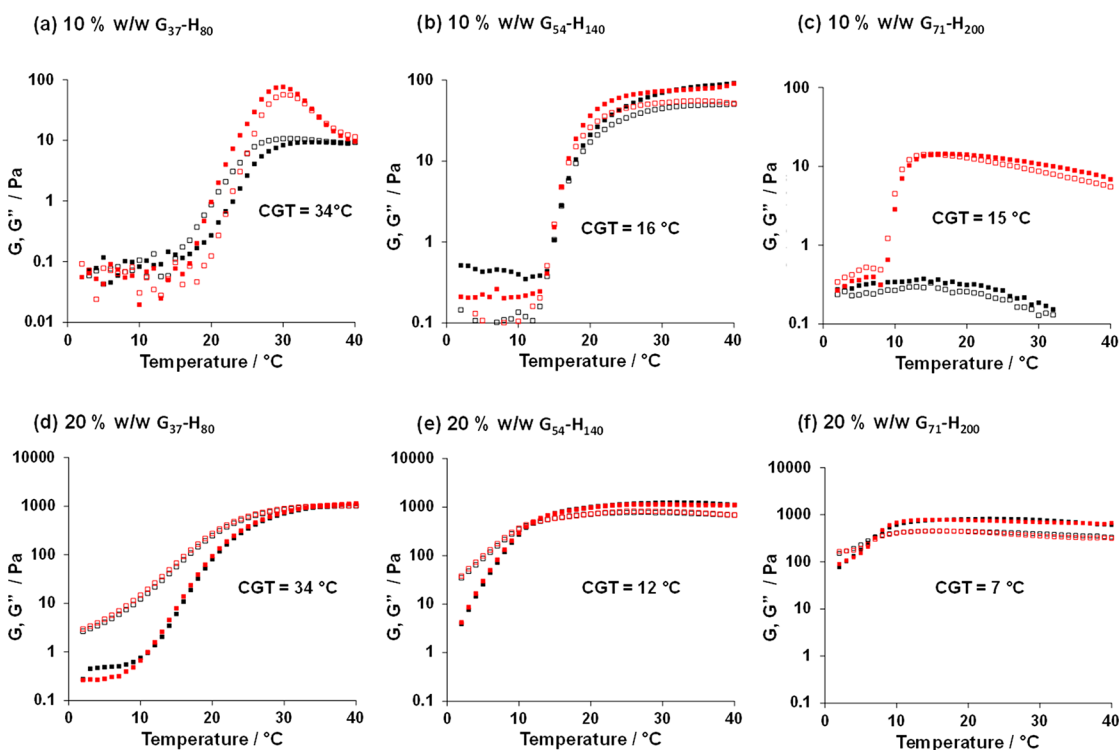


**Figure 7.** Temperature-dependent oscillatory rheology studies obtained on cooling (red data) and heating (black data) aqueous dispersions of three types of  $G_x$ - $H_y$  worms: (a) 10% w/w  $G_{37}$ - $H_{80}$ , (b) 10% w/w  $G_{54}$ - $H_{140}$ , (c) 10% w/w  $G_{71}$ - $H_{200}$ , (d) 20% w/w  $G_{37}$ - $H_{80}$ , (e) 20% w/w  $G_{54}$ - $H_{140}$ , and (f) 20% w/w  $G_{71}$ - $H_{200}$ . Closed symbols represent  $G'$ , and open symbols represent  $G''$ . Oscillatory shear conditions: angular frequency = 10 rad  $s^{-1}$ , applied strain amplitude = 1.0%.

correlation with the TEM observations (Figure 3). Interestingly,  $L_k$  also increases with molecular weight; this latter parameter provides an indication of the worm stiffness. Hence,

higher copolymer molecular weights lead to less flexible worms, presumably owing to the greater degree of chain entanglements for the PHPMA blocks within the worm cores.

**Variable Temperature Studies.** The thermal response of the  $G_x$ - $H_y$  copolymer dispersions was initially tested by conducting variable temperature DLS studies on 0.1% w/w aqueous dispersions of the  $G_{37}$ - $H_{80}$ ,  $G_{54}$ - $H_{140}$ , and  $G_{71}$ - $H_{200}$  worms (Figure 6). The  $G_{37}$ - $H_{80}$  worms had a “sphere-equivalent”  $z$ -average diameter of 60 nm at 40 °C, which suggests the presence of relatively short worms and perhaps also some spherical dimers or trimers (Figure 6a).<sup>8</sup> On cooling to 15 °C, a gradual reduction in  $z$ -average diameter to 35 nm was observed, which suggests at least partial worm breakup to produce mainly spheres. Below 15 °C, the scattered light intensity became much weaker and the particle size data became less reliable, which is consistent with the formation of *molecularly dissolved* copolymer chains. Similar observations were made by Kocik and co-workers, who used SAXS to study a  $G_{57}$ - $H_{140}$  diblock copolymer at subambient temperature and estimated an aggregation number of 4 at 2 °C.<sup>57</sup>

In this study, the change in  $G_{37}$ - $H_{80}$  copolymer morphology is fully reversible, with no discernible hysteresis. Presumably, its relatively low molecular weight favors dynamic exchange of copolymer chains. In this context, it is noteworthy that Blanazs and co-workers reported that a PHPMA DP of 92 was required to induce micellar aggregation during the RAFT aqueous dispersion polymerization of HPMA.<sup>30</sup> Moreover, during such PISA syntheses the unreacted HPMA monomer is expected to act as a cosolvent for the growing weakly hydrophobic PHPMA chains, thus delaying the onset of nucleation. Hence, the DP of the weakly hydrophobic block in the  $G_{37}$ - $H_{80}$  copolymer most likely lies close to the minimum value required for micellar self-assembly.

For a 0.1% w/w aqueous dispersion of  $G_{54}$ - $H_{140}$  worms, DLS studies indicated that an initial “sphere-equivalent” diameter of 390 nm at 40 °C was reduced to 45 nm at 9 °C, suggesting a worm-to-sphere transition. Further cooling to 2 °C resulted in a low count rate producing erratic DLS results. On heating this sample, a constant size of ~48 nm was recorded, indicating the worms were not re-formed, instead remaining as kinetically trapped spheres throughout the heating ramp. The reduction in size also occurred for the 0.1% w/w aqueous dispersion of  $G_{71}$ - $H_{200}$  worms (Figure 6c), where the sphere-equivalent diameter reduced from 284 to ~45 nm at 2 °C. Interestingly, erratic values for the size were not observed at low temperatures for this sample, presumably due to the high molecular weight of the copolymer preventing dissolution. Again, no increase in size occurred during the heating cycle. This indicates that the spheres remain kinetically trapped under such conditions, presumably because the longer PGMA block confers sufficient steric stabilization to prevent efficient sphere–sphere fusion, at least on normal experimental time scales. Similar hysteresis has been reported previously for  $G_x$ - $H_y$  PHPMA worms<sup>21</sup> and other stimulus-responsive micellar systems.<sup>32,68–71</sup> This most likely reflects the highly cooperative nature of the sphere–sphere fusion events that are required to re-form the worms during the heating cycle. In contrast, worm dissociation to form spheres most likely proceeds via a concentration-independent “worm budding” mechanism, as described by Fielding and co-workers.<sup>28</sup>

Oscillatory rheology studies conducted on the three worm gels at copolymer concentrations of 10% w/w (Figure 7a–c) and 20% w/w (Figure 7d–f) confirmed their thermoresponsive nature in each case. At 10% w/w, the  $G_{54}$ - $H_{140}$  worm dispersion underwent degelation on cooling from 40 to 2 °C followed by regelation on returning to 40 °C, as previously

reported.<sup>21</sup> The critical gelation temperature (CGT, which is defined as the crossover temperature for the  $G'$  and  $G''$  curves) was determined to be 15 °C on cooling and 16 °C on heating. This represents rather milder hysteresis than that observed during the variable temperature DLS experiments, performed on dispersions with low copolymer concentration, but again suggests that worm dissociation occurs more readily than sphere–sphere fusion. Interestingly, the  $G_{71}$ - $H_{200}$  worms exhibit qualitatively different behavior at the same 10% w/w copolymer concentration: a CGT of 16 °C was observed on cooling, but regelation did not occur on the time scale of this rheology experiment, which involved an equilibration time of 3 min at each temperature. Clearly, the longer PGMA block confers more effective steric stabilization, which impedes sphere–sphere fusion. Moreover, the longer PHPMA block is more hydrophobic and hence less thermoresponsive.<sup>72–74</sup> Similar behavior has been reported for PEG-PHPMA<sup>41</sup> and PSBMA-PHPMA<sup>31</sup> PISA formulations possessing PHPMA blocks of comparable DP.

On cooling a 10% w/w  $G_{37}$ - $H_{80}$  worm dispersion from 40 to 29 °C, an *increase* in both  $G'$  and  $G''$  was observed, followed by the anticipated reduction on further cooling. Bearing in mind observations made by Verber et al.,<sup>21</sup> such maxima most likely correspond to the formation of highly linear worms at around 29 °C, with branched worms and/or worm clusters being initially present at 40 °C which are break up on shear. These  $G_{37}$ - $H_{80}$  worms eventually undergo the expected worm-to-sphere transition (and hence degelation) on cooling. However, although both  $G'$  and  $G''$  increase on heating this dispersion, a CGT is not observed until 34 °C.

To observe fully reversible (de)gelation behavior for all three worm dispersions, the copolymer concentration had to be increased up to 20% w/w (Figure 7d–f). This also eliminated hysteresis, since sphere–sphere fusion becomes more favorable at such a high copolymer concentration. However, although degelation occurs on cooling, the cold free-flowing  $G_{54}$ - $HP_{140}$  and  $G_{71}$ - $H_{200}$  dispersions remain relatively viscous at 2 °C, even after equilibration overnight (>16 h). This indicates the presence of short worms, which suggests that the worm-to-sphere transition is not complete at this relatively high copolymer concentration. This observation is supported in the rheo-optical studies discussed later.

Such rheology measurements enable  $\tan \delta$  to be calculated, where  $\tan \delta = G''/G'$  and  $G'$  and  $G''$  represent the energy per unit strain that is either stored or dissipated within these worm gels.<sup>75</sup> Examining the angular frequency dependence of  $G'$  and  $G''$  of each worm dispersion at temperatures above the CGT where the gel moduli plateau (Figure S6) enabled determination of  $\tan \delta$ . At 10 rad  $s^{-1}$ , the  $G_{37}$ - $H_{80}$ ,  $G_{54}$ - $H_{140}$ , and  $G_{71}$ - $H_{200}$  worm dispersions exhibited  $\tan \delta$  values of 0.94 at 35 °C, 0.74 at 25 °C, and 0.55 at 25 °C, respectively. This systematic reduction indicates less efficient energy dissipation with increasing copolymer molecular weight. The lower molecular weight chains are likely to be less entangled and hence more mobile within the worm cores, allowing relatively efficient energy dissipation compared to the more entangled higher molecular weight chains. Moreover, the  $G_{37}$ - $H_{80}$  copolymer worms are likely to undergo dissociation and re-formation under shear, as reported for conventional low molecular weight surfactant worms.<sup>76</sup> This would provide an additional energy dissipation mechanism, which is not available for the higher molecular weight copolymer worms.

Previous studies on  $G_{54}$ - $H_{140}$  worms indicated that systematically reducing the copolymer concentration to  $\sim 4.0\%$  w/w led to physical degelation, as judged by rheological measurements.<sup>21</sup> Below this critical gelation concentration (CGC),  $G'$  remained below  $G''$  at all temperatures. In these earlier experiments, it was not possible to directly determine the morphology at this copolymer concentration because TEM and DLS both require a significantly lower copolymer concentration ( $\leq 0.2\%$  w/w). In contrast, SAXS enables the copolymer morphology to be determined over the 1–5% w/w concentration range. After equilibration at 25 °C for 24 h, SAXS patterns were recorded over a range of copolymer concentrations (Figure 8 and Figure S7a). At this temperature,

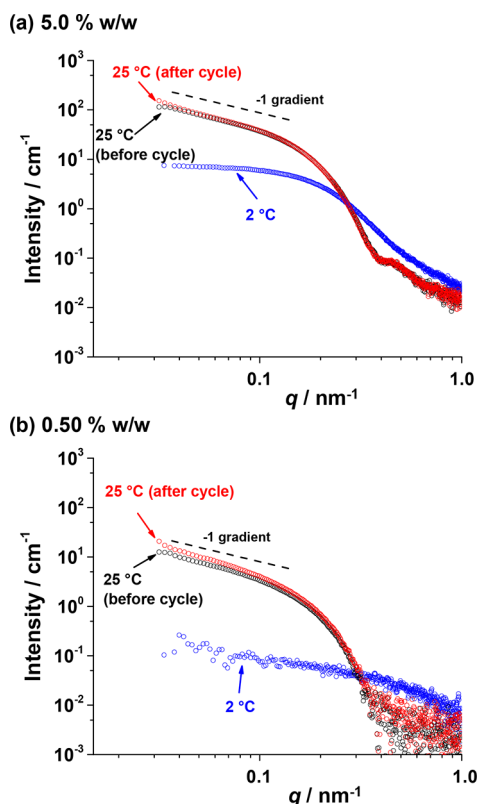


**Figure 8.** Representative small-angle X-ray scattering (SAXS) patterns recorded for aqueous dispersions of a  $G_{54}$ - $H_{140}$  diblock copolymer (a) at 5.0% w/w and (b) 0.50% w/w. Black data were recorded at 25 °C before conducting the thermal cycle. Blue data were obtained after cooling to 2 °C and equilibrating for 30 min. Red data were recorded after reheating to 25 °C and equilibrating for 24 h. A gradient of  $-1$  is provided as a guide for the eye. A full set of SAXS data for various sample concentrations is given in the Supporting Information (Figure S7).

SAXS patterns exhibited a gradient of  $\sim -1$  at low  $q$ , indicating a rodlike morphology,<sup>77</sup> and also a feature at higher  $q$  ( $\sim 0.4 \text{ nm}^{-1}$ ), corresponding to the worm cross-sectional diameter. These observations confirm that dilution of this copolymer composition at ambient temperature has no effect on the worm morphology. Hence, the physical degelation that occurs below the CGC of around 4.0% w/w does not indicate loss of the worm morphology; instead, it simply indicates that there are no longer sufficient interworm contacts to maintain a 3D gel network.<sup>53</sup> However, qualitatively different behavior was observed for each copolymer concentration on cooling to 2 °C (Figure 7 and Figure S7b). Each SAXS pattern recorded at this subambient

temperature exhibited a low  $q$  gradient of close to zero at concentrations of 2.0% w/w copolymer and above, indicating the presence of spheres (and possibly, minor populations of dimers and trimers).<sup>8,77</sup> At 0.5% w/w copolymer concentration (Figure 8b), a significant reduction in X-ray scattering intensity was observed at 2 °C at low  $q$  with a concomitant increase at higher  $q$ . This suggests a further morphology transition from spheres to weakly interacting chains.<sup>40</sup> This is not surprising given that the PHPMA block becomes more solvated (i.e., less hydrophobic) at lower temperature.<sup>8</sup>

On returning to 25 °C and equilibrating for 24 h, the SAXS pattern recorded for the aqueous  $G_{54}$ - $H_{140}$  dispersion after this thermal cycle was more or less superimposable on the original pattern, indicating that the original worms are eventually reconstituted even at copolymer concentrations as low as 0.50% w/w (Figure 7 and Figure S7c). These observations differ from those made during the variable temperature DLS studies, which indicated that over the time scale of the experiment the worm-to-sphere transition was irreversible at 0.1% w/w. Perhaps, a 5-fold difference in copolymer concentration in these experiments significantly reduces the probability of worm reconstitution.

Temperature-dependent SAXS measurements were also conducted on a 5.0% w/w  $G_{54}$ - $H_{140}$  copolymer dispersion to study the sphere-to-worm transition (Figure 9). This

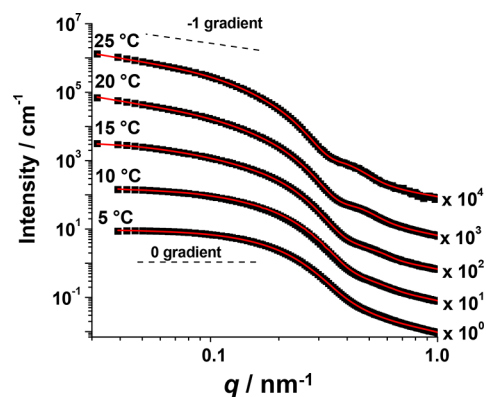


**Figure 9.** Small-angle X-ray scattering (SAXS) patterns obtained for a 5.0% w/w aqueous dispersion of  $G_{54}$ - $H_{140}$  diblock copolymer nano-objects recorded on heating from 5 to 25 °C. The red solid lines are calculated fits to the data using a combination of spherical micelle and wormlike micelle models. Gradients of 0 and  $-1$  are provided as guidance for the eye. Each SAXS pattern is offset by an arbitrary multiplication factor (shown at the right side of the patterns) for clarity. These data confirm a fully reversible sphere-to-worm transition for this copolymer under the stated conditions.

copolymer concentration was chosen to ensure fully reversible gelation while minimizing the structure factor contribution to the scattering pattern, which can otherwise complicate data analysis. The SAXS pattern recorded at 5 °C for  $G_{54}$ - $H_{140}$  exhibited a zero gradient at low  $q$ , as expected for spheres. On heating, a gradual change is observed at around  $q = 0.4 \text{ nm}^{-1}$ , where this feature corresponds to either the sphere diameter,  $d_s$ , or the worm core cross-sectional diameter,  $d_w$  (see schematic representation in Figure 5). In addition, the gradient at low  $q$  tends toward  $-1$  at higher temperature, which indicates the formation of highly anisotropic/cylindrical nanoparticles (i.e., worms).<sup>77</sup> These SAXS patterns were fitted to worm micelle and/or spherical micelle models<sup>28</sup> to extract further structural information. The 5 °C pattern easily fit a



spherical micelle model alone, but measurements above this temperature required a two-population (i.e., sphere plus worm) model to obtain satisfactory data fits.

Between 10 and 20 °C, the worm contour length,  $L_c$ , increases from 96 nm at 10 °C to 521 nm at 20 °C (Figure 10). At higher temperatures, it was not possible to obtain a

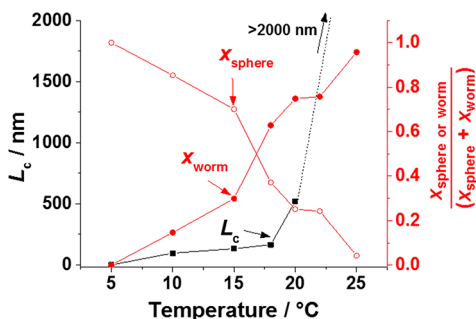


**Figure 10.** Temperature dependence of the mean worm contour length,  $L_c$  (black squares), and the relative volume fraction of the copolymer in the solution comprising worms ( $x_{\text{worm}}$ ; solid red circles) and spheres ( $x_{\text{sphere}}$ ; hollow red circles) determined by SAXS for a 5.0% w/w aqueous dispersion of a  $G_{54}\text{-H}_{140}$  diblock copolymer. Lines are a guide for the eye.

reliable value for  $L_c$  since it is beyond the recorded  $q$  range. However, it is reasonable to state that  $L_c$  is over 2000 nm in each case (Figure 10). Fitting both populations also enables the relative volume fraction of polymer forming either worms ( $x_{\text{worm}}$ ) or spheres ( $x_{\text{sphere}}$ ) to be calculated for each temperature. A gradual increase in  $x_{\text{worm}}$  at the expense of spheres is observed from 10 to 25 °C, at which 95% of the polymer forms worms. These observations suggest that the mechanism for the morphological evolution from spheres to worms involves multiple 1D fusion events between each species. Such SAXS observations, where  $x_{\text{worm}}$  and  $L_c$  are increasing are consistent with the increase in viscosity/gel strength observed during rheological experiments. The effect of varying  $L_c$  on gel strength has also been observed for surfactant worms<sup>78</sup> and has been recently rationalized in the context of percolation theory for this particular polymer formulation by Lovett and co-workers.<sup>53</sup>

Above 25 °C, it was much more difficult to achieve a satisfactory fit to the data. In principle, this may indicate further morphological evolution and this tentative explanation is investigated later.

#### Shear-Induced Polarized Light Imaging Studies.

SIPLI is a relatively new technique that has proven to be a powerful tool for studying the structural alignments and phase transitions under shear.<sup>61,62</sup> In the present work, variable-temperature SIPLI studies are used to assess the rheological behavior of the three aqueous copolymer dispersions. At 2 °C, a 5.0% w/w dispersion of  $G_{54}\text{-H}_{140}$  exists as a free-flowing dispersion of spheres with an apparent viscosity of 0.1 Pa·s, which is comparable to that of water (Figure 11a). During a continuous heating ramp, the viscosity remained relatively constant up to 23 °C; thereafter, higher viscosities indicated the formation of anisotropic worms. Indeed, a characteristic Maltese cross appeared in the polarized light images (Figure 11b) at 26 °C, which indicated birefringence caused by worm alignment under shear.<sup>61</sup> The observations roughly correspond to those in the temperature-dependent SAXS study, where a

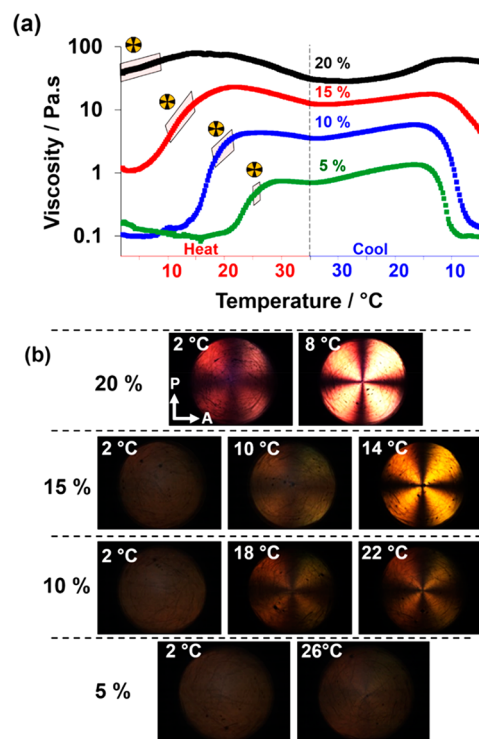


**Figure 11.** (a) Viscosity vs temperature plots obtained from continuous shear rheology studies conducted on  $G_{54}\text{-H}_{140}$  copolymer dispersions at concentrations of 5% w/w (green symbols), 10% w/w (blue symbols), 15% w/w (red symbols), and 20% w/w (black symbols). The shaded region indicates the temperature range in which the characteristic Maltese cross was observed during the heating cycle. For the 5% w/w worm dispersion, the Maltese cross was only visible at 26 °C. (b) SIPLI images obtained at various temperatures during a thermal cycle conducted for  $G_{54}\text{-H}_{140}$  worms at copolymer concentrations of 5, 10, 15, or 20% w/w. The Maltese cross indicates birefringence, which is the result of worm alignment under a shear flow. Arrows on PLI indicate orientation of the polarizer (P) and the analyzer (A).

population of relatively long worms (contour length >2000 nm) is detected between 20 and 25 °C.

However, the Maltese cross feature was rather weak at this relatively low copolymer concentration. It also disappeared at higher temperature, which coincided with a plateau in viscosity just below 1.0 Pa·s. On cooling, an abrupt reduction in viscosity was observed at 15 °C, indicating a worm-to-sphere transition. This dissociative process proceeds much faster than the associative formation of worms since the latter requires a cooperative mechanism (i.e., the 1D fusion of multiple spheres).

In view of the relatively poor contrast, the  $G_{54}\text{-H}_{140}$  copolymer concentration was increased to 10% w/w. A similar viscosity vs temperature profile was observed, albeit with a lower onset temperature for the upturn in viscosity and a somewhat higher plateau viscosity (3 Pa·s). Moreover, more intense polarized light images were obtained between 18 and 22 °C, which coincided with the greatest increase in viscosity. At a copolymer concentration of either 15% or 20% w/w, the dispersion exhibited an apparent viscosity of 1 or 34 Pa·s, respectively, at 2 °C, which was consistent with oscillatory rheology studies (Figure 7e). This suggests that the copolymer morphology is concentration-dependent. This phenomenon has been observed before for poly(ethylene oxide)–poly-

(propylene oxide) block copolymers exhibiting concentration-dependent morphology transitions.<sup>79</sup>

Interestingly, in all cases, the plateau in viscosity coincided with the disappearance of the Maltese cross under these conditions, suggesting that shear-induced worm alignment is disrupted. Thus, a further SIPLI experiment was conducted on the 10% w/w  $G_{54}$ - $H_{140}$  worms at a lower angular speed of  $0.08 \text{ rad s}^{-1}$ . In this case, an increase in viscosity was observed at higher temperatures, along with a distorted Maltese cross (see Figure 12). Both observations suggest worm branching, and

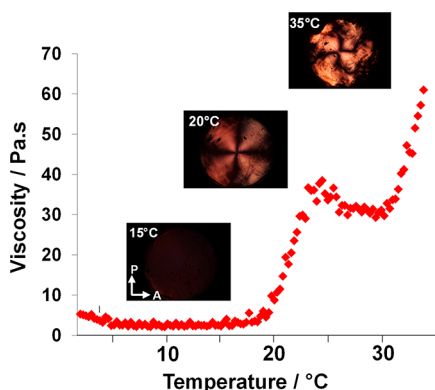


**Figure 12.** Viscosity vs temperature recorded for a 10% w/w  $G_{54}$ - $H_{140}$  worm gel while shearing at  $1 \text{ s}^{-1}$ . Inset: SIPLI images recorded at 35, 20, and 15 °C during the temperature ramp. Arrows on PLI indicate orientation of the polarizer (P) and the analyzer (A)

this hypothesis is also consistent with a USAXS pattern recorded for a 5.0% w/w aqueous dispersion of  $G_{54}$ - $H_{140}$

worms at 35 °C (see Figure S9). USAXS enables scattering at extremely low  $q$  to be obtained, which is a prerequisite to determine the presence of branching.<sup>80</sup> Within this pattern a transition from the  $q^{-1}$  regime of scattering intensity dependence to a higher gradient at  $q \sim 0.03 \text{ nm}^{-1}$  is noticeable. A similar result has been reported for branched worms formed by a surfactant,<sup>80</sup> but further studies are warranted to confirm both the presence and extent of worm branching.

SIPLI experiments were also conducted on 20% w/w aqueous dispersions of  $G_{37}$ - $H_{80}$  and  $G_{71}$ - $H_{200}$  worms (Figure 13). The former dispersion forms a free-flowing, low-viscosity liquid at 2 °C but is transformed into a viscous gel at 25 °C, with further heating to 35 °C leading to a reduction in viscosity. When sheared at an angular speed of  $0.8 \text{ rad s}^{-1}$  no birefringence was observed at 2 °C, as expected for a dispersion of spherical nanoparticles. At 25 °C, polarized light imaging revealed a partial Maltese cross for the  $G_{37}$ - $H_{80}$  dispersion, where shear alignment is only observed above a specific radial displacement from the center of the geometry. The observed boundary corresponds to a minimum shear rate  $\dot{\gamma}_b$  required for the orientation of worms along the flow direction. This is due to the fact that the worm relaxation time ( $\tau$ ) is somewhat faster in comparison to the shear flow rate inside the dark central area ( $\dot{\gamma} < \dot{\gamma}_b = \frac{1}{\tau}$ ). As a consequence, the worm micelles are not oriented and the dispersion is nonbirefringent in the central region of the sample. The edge of the dark area corresponds to a shear rate of  $\sim 1 \text{ s}^{-1}$  (where  $\dot{\gamma} = \frac{\omega r}{h}$ ; see Figure S8 for further details); hence, the worm relaxation time, which is the reciprocal of the minimum shear rate required for alignment, is of the order of 1 s. A radius of

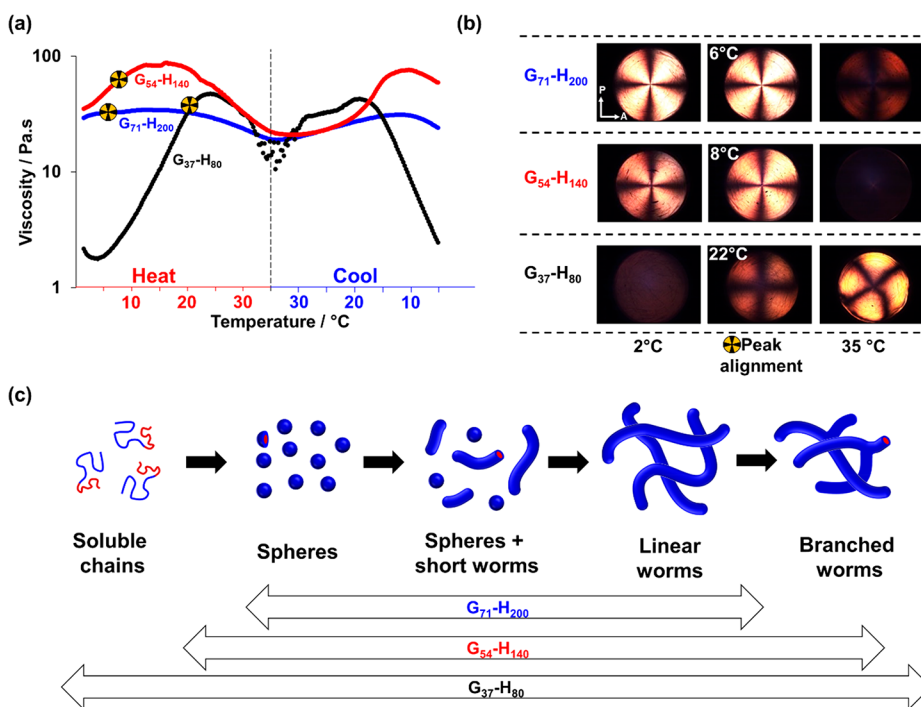


**Figure 13.** (a) Viscosity vs temperature plots recorded for 20% w/w aqueous dispersions of the three  $G_x$ - $H_y$  diblock copolymers examined in this study. Maltese cross symbols indicate the temperature at which maximum worm alignment was observed. (b) SIPLI images obtained at 2 °C (the first column), at the characteristic temperature where the Maltese cross was judged to be most intense (i.e., 6, 8, or 22 °C) (the second column), and at 35 °C (the third column). Arrows on PLI indicate orientation of the polarizer (P) and the analyzer (A). (c) Schematic representation of the proposed mechanism for the transition from spheres to worms to branched worms that occurs on raising the temperature from 5 to 35 °C.

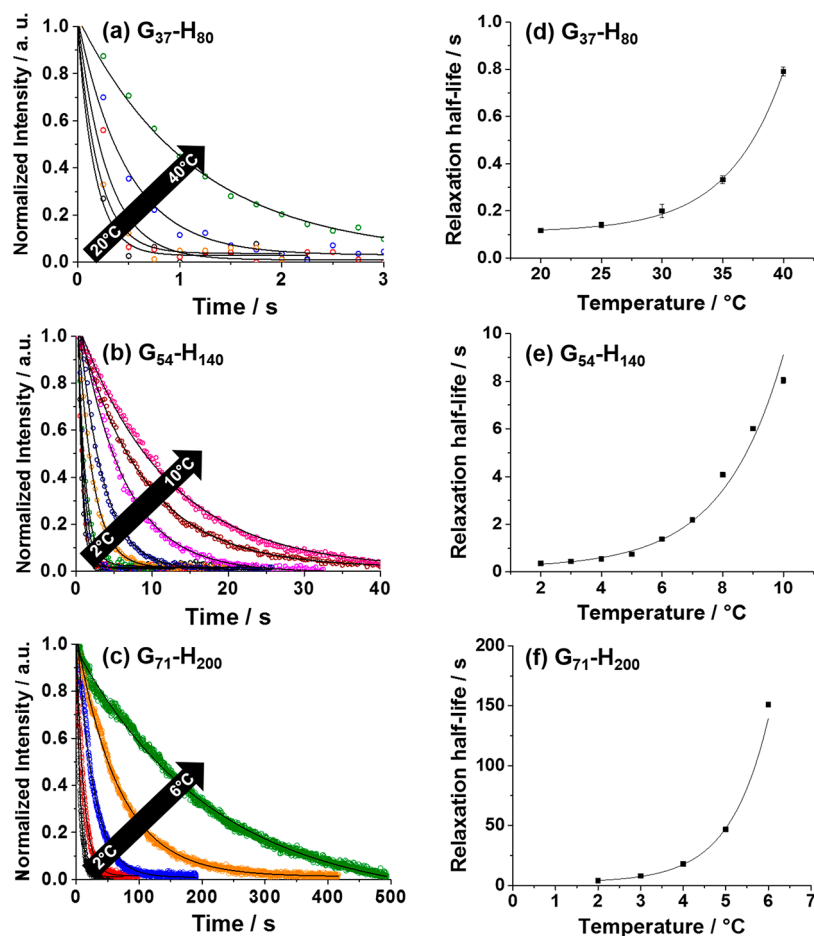


**Figure 14.** SIPLI relaxation studies conducted on 20% w/w aqueous dispersions of  $G_{37}\text{-H}_{80}$ ,  $G_{54}\text{-H}_{140}$ , and  $G_{71}\text{-H}_{200}$  worms at various temperatures (20–40, 2–10, and 2–6 °C, respectively): (a–c) show the decay of the image intensity vs time after cessation of shear (the solid line represents a fit to an exponential decay); (d–f) show the temperature dependence of the characteristic half-life time,  $\tau_{1/2}$ , required for worm relaxation (here the solid lines are merely a guide for the eye).

the dark central area in the PLIs corresponding to  $G_{54}\text{-H}_{140}$  and  $G_{71}\text{-H}_{200}$  worms is very small in a comparison with the  $G_{71}\text{-H}_{200}$  worms (Figure 13b). This suggests that the boundary shear rate required for the orientation of these worms is significantly less than for  $G_{37}\text{-H}_{80}$  worms and cannot be resolved in images obtained with the used angular speed. Thus, the relaxation times of thick  $G_{54}\text{-H}_{140}$  and  $G_{71}\text{-H}_{200}$  worms are longer than the relaxation time for the thinner  $G_{37}\text{-H}_{80}$  worms.

20% w/w aqueous dispersion of  $G_{71}\text{-H}_{200}$  worms forms a viscous liquid at 2 °C but exhibits only a rather modest increase in viscosity at higher temperatures. Nevertheless, a viscosity maximum was observed at around 15 °C (Figure 13). At 35 °C, qualitative differences were observed between the three types of copolymer worms. A faint Maltese cross was visible for  $G_{71}\text{-H}_{200}$  (Figure 13b), no cross was observed for  $G_{54}\text{-H}_{140}$  worms, while an intense, distorted Maltese cross was obtained for  $G_{37}\text{-H}_{80}$  worms. This suggests that longer PHPMA blocks are more hydrophobic and less plasticized by water and hence exhibit lower chain mobility. This restricts the ability of the  $G_{71}\text{-H}_{200}$  worms to undergo a thermally induced morphological transition (see Figure 13c). Moreover, the relatively long  $G_{71}$  stabilizer block provides a more effective steric barrier to the multiple sphere–sphere fusion events that are required for efficient worm reconstitution on returning to ambient temperature. In contrast, the  $G_{54}\text{-H}_{140}$  worms comprise PHPMA chains that are sufficiently mobile to

undergo thermoreversible (de)gelation with minimal hysteresis as well as some degree of branching, with the latter leading to an increase in viscosity at higher temperatures under gentle shear (Figure 12). The shorter, surfactant-like  $G_{37}\text{-H}_{80}$  chains are even more mobile and hence may be able to form higher order morphologies such as lamellar sheets. This possibility warrants further study but is beyond the scope of the current work.

**Worm Relaxation Studies.** SIPLI also provides a convenient means of measuring the rate of relaxation of aligned worms on cessation of shear by timing the disappearance of the Maltese cross motif. Such time-resolved experiments were conducted over a range of temperatures for each of the three copolymer worm dispersions at 20% w/w (Figure 14). This concentration was used since the linear worms persisted over a broad temperature range as judged by the appearance of a Maltese cross on applying shear. Furthermore, this motif was most intense in the 20% w/w samples, meaning analysis was more straightforward.

Dispersions were presheared continuously by parallel plate rotational geometry using angular speed of 0.8 rad s<sup>-1</sup> for 60 s. After the ceasing rotation, the force which aligns the worms is removed and the worms can relax. This is observed visually by the reduction in intensity and eventual disappearance of the Maltese cross in the PLIs. Analysis of a sequence of images captured every 250 ms after stopping the shear provided a

convenient means to quantify the relaxation dynamics. Using image analysis software, the sequential time-resolved images were stacked and sliced perpendicular to the imaging plane (see also Figure S8a,b for details). By plotting the reduction in light intensity from the point of cessation of shear, a decay curve is produced (Figure 14a–c) from which it is possible to extract a characteristic relaxation time,  $\tau_1$ , and the associated half-life time,  $\tau_{1/2}$ . In principle,  $\tau_{1/2}$  values should depend on parameters such as mean worm contour length, worm diameter, degree of worm branching/clustering, and the overall copolymer molecular weight. Unfortunately, it would be difficult to make meaningful comparisons between the three worm dispersions examined in this study. This problem can be partially mitigated by conducting measurements over the entire temperature range for which a Maltese cross is visible. It is then assumed that this temperature range corresponds to the presence of linear worms. Within this temperature range, longer relaxation times are observed at higher temperatures, indicating the presence of longer worms.

At a certain critical temperature, the Maltese cross becomes distorted and eventually disappears, most likely indicating the formation of branched worms that cannot undergo shear-induced alignment. Similar behavior is observed for all three copolymer worms, but the absolute time scales for relaxation differ considerably. The characteristic relaxation half-lives obtained for  $G_{37}\text{-}H_{80}$  worms were very short (see Figure 14a) with half-lives ranging from less than 0.20 s at 20 °C up to 0.80 s at 40 °C. Such findings are consistent with the estimated relaxation time of 1.0 s obtained from the SIPLI study of this copolymer dispersion (see Figure S8, calculated from the minimum shear rate required for worm alignment). For the  $G_{54}\text{-}H_{140}$  and  $G_{71}\text{-}H_{200}$  worms, the relaxation times were significantly longer (Figure 14b,c). Thus, relaxation times ranged from less than 0.50 s at 2 °C to 8.0 s at 8 °C for  $G_{54}\text{-}H_{140}$  worms and from 1.0 to 150 s for  $G_{71}\text{-}H_{200}$  worms (Figure 14e,f). In general, these observations clearly demonstrate that the copolymer molecular weight strongly influences the mean relaxation time of the assembled worms. Presumably, this reflects the larger number of interchain entanglements within the worm cores, which constrain chain mobility and hence increase the worm relaxation time.

## CONCLUSIONS

By use of an appropriate phase diagram, a series of  $G_x\text{-}H_y$  diblock copolymer worms of varying copolymer molecular weight and, consequently, cross-sectional diameter can be prepared by RAFT aqueous dispersion polymerization of HPMA. This was achieved by varying the mean DP for the hydrophilic PGMA stabilizer block and then extending such macro-CTAs while targeting an appropriate DP for the hydrophobic PHPMA block. DMF GPC analysis revealed the expected systematic variation in copolymer molecular weight, while TEM and SAXS studies confirmed that a pure worm phase was obtained in each case (with a gradual increase in worm cross-sectional diameter). Importantly, the precise thermoresponsive behavior exhibited by such worms is critically dependent on their copolymer molecular weight.

DLS studies of a 0.1% w/w dispersion of  $G_{37}\text{-}H_{80}$  worms reveal fully reversible worm-to-sphere and sphere-to-unimer transitions on cooling to 2 °C. In contrast, the worm-to-sphere transition observed for the  $G_{54}\text{-}H_{140}$  and  $G_{71}\text{-}H_{200}$  at the same concentration proved to be irreversible over the experimental time scale, with no evidence for the sphere-to-worm transition

occurring on reverse heating. At a copolymer concentration of 10% w/w, rheology studies demonstrated that (de)gelation was fully reversible for  $G_{37}\text{-}H_{80}$  and  $G_{54}\text{-}H_{140}$  but irreversible for  $G_{71}\text{-}H_{200}$ . Increasing the copolymer concentration to 20% w/w produced a reversible thermal transition in each case. However, the gel moduli were independent of copolymer molecular weight under these conditions, suggesting that this parameter is primarily determined by interworm interactions and/or the bulk modulus of the worm cores. Much slower thermal transitions occur when using longer PHPMA blocks, which is consistent with the irreversible degelation behavior observed for a series of closely related PEG-PHPMA block copolymers. Hence, with the benefit of hindsight, our earlier reports of rapid thermoreversible gelation, which has potential biomedical applications,<sup>43,55,58,59</sup> were somewhat serendipitous.

SAXS studies confirmed that the worm-to-sphere transition for the  $G_{54}\text{-}H_{140}$  nano-objects is reversible at copolymer concentrations as low as 0.5% w/w if a sufficiently long equilibration time is allowed. SAXS patterns recorded from 5 to 25 °C for a 5.0% w/w aqueous dispersion of  $G_{54}\text{-}H_{140}$  worms could be satisfactorily fitted using a “sphere plus worm” two-population model. This analysis indicated that worms grow longer at the expense of the spheres at higher temperature. This suggests that the sphere-to-worm transition most likely occurs via 1D sphere–worm fusion. Continuous shear rheology measurements indicate a maximum in dispersion viscosity at 22 °C, which is attributed to an increase in worm contour length and worm volume fraction. The lower viscosities observed above 22 °C coincide with an apparent reduction in the worm contour length indicated by SAXS, but additional USAXS data provide evidence for worm branching. This is consistent with SIPLI studies, which indicate an upturn in viscosity at low shear rates. Finally, relaxation studies indicate that the copolymer molecular weight (and hence worm cross-sectional diameter) is an important parameter: relatively thin  $G_{37}\text{-}H_{80}$  worms relax much faster after their shear alignment (half-life <1 s) than relatively thick  $G_{71}\text{-}H_{200}$  worms (half-lives ~10–150 s).

## ASSOCIATED CONTENT

### Supporting Information

The Supporting Information is available free of charge on the ACS Publications website at DOI: 10.1021/acs.macromol.8b01617.

Summary table for  $G_x$  macro-CTAs; NMR spectra; oscillatory rheology frequency sweeps; additional SAXS and USAXS patterns; SIPLI image processing and SAXS model details (PDF)

## AUTHOR INFORMATION

### Corresponding Authors

\*E-mail s.p.armes@shef.ac.uk (S.P.A.).

\*E-mail n.warren@leeds.ac.uk (N.J.W.).

### ORCID

Nicholas J. Warren: 0000-0002-8298-1417

Matthew J. Derry: 0000-0001-5010-6725

Oleksandr O. Mykhaylyk: 0000-0003-4110-8328

Vincent Admiral: 0000-0002-7590-4800

Steven P. Armes: 0000-0002-8289-6351

## Notes

The authors declare no competing financial interest.

## ACKNOWLEDGMENTS

We are grateful to the ESRF (beamline ID02) and Diamond Light Source (beamline I22) for providing synchrotron beam time and thank the personnel for their assistance. EPSRC is thanked for postdoctoral support of N.J.W. (EP/L024160/1) and also for a Platform grant (EP/J007846/1) to support M.J.D., A.B., V.L., L.R., and O.O.M. O.O.M. and S.P.A. are grateful to EPSRC for a capital equipment grant to purchase the Xenocs/Excillum SAXS laboratory instrument (EP/M028437/1). GEO Specialty Chemicals (Hythe, UK) is thanked for supplying the GMA and HEMA monomers and also for part-funding a PhD studentship for J.R.L. S.P.A. is the recipient of a five-year ERC Advanced Investigator grant (PISA 320372) and also an EPSRC Established Career Particle Technology Fellowship (R/003009/1).

## REFERENCES

- (1) Mai, Y.; Eisenberg, A. Self-assembly of block copolymers. *Chem. Soc. Rev.* **2012**, *41* (18), 5969–5985.
- (2) Blanazs, A.; Armes, S. P.; Ryan, A. J. Self-Assembled Block Copolymer Aggregates: From Micelles to Vesicles and their Biological Applications. *Macromol. Rapid Commun.* **2009**, *30* (4–5), 267–277.
- (3) Zhang, L.; Eisenberg, A. Multiple Morphologies of “Crew-Cut” Aggregates of Polystyrene-*b*-poly(acrylic acid) Block Copolymers. *Science* **1995**, *268* (5218), 1728–1731.
- (4) Bütün, V.; Armes, S. P.; Billingham, N. C. Synthesis and aqueous solution properties of near-monodisperse tertiary amine methacrylate homopolymers and diblock copolymers. *Polymer* **2001**, *42* (14), 5993–6008.
- (5) Pearson, R. T.; Warren, N. J.; Lewis, A. L.; Armes, S. P.; Battaglia, G. Effect of pH and Temperature on PMPC–PDPA Copolymer Self-Assembly. *Macromolecules* **2013**, *46* (4), 1400–1407.
- (6) Howse, J. R.; Jones, R. A. L.; Battaglia, G.; Ducker, R. E.; Leggett, G. J.; Ryan, A. J. Templated formation of giant polymer vesicles with controlled size distributions. *Nat. Mater.* **2009**, *8* (6), 507–511.
- (7) Israelachvili, J. N.; Mitchell, D. J.; Ninham, B. W. Theory of self-assembly of hydrocarbon amphiphiles into micelles and bilayers. *J. Chem. Soc., Faraday Trans. 2* **1976**, *72* (0), 1525–1568.
- (8) Blanazs, A.; Verber, R.; Mykhaylyk, O. O.; Ryan, A. J.; Heath, J. Z.; Douglas, C. W. I.; Armes, S. P. Sterilizable Gels from Thermo-responsive Block Copolymer Worms. *J. Am. Chem. Soc.* **2012**, *134* (23), 9741–9748.
- (9) Jia, Z.; Bobrin, V. A.; Truong, N. P.; Gillard, M.; Monteiro, M. J. Multifunctional Nanoworms and Nanorods through a One-Step Aqueous Dispersion Polymerization. *J. Am. Chem. Soc.* **2014**, *136* (16), 5824–5827.
- (10) Massey, J. A.; Temple, K.; Cao, L.; Rharbi, Y.; Ruez, J.; Winnik, M. A.; Manners, I. Self-Assembly of Organometallic Block Copolymers: The Role of Crystallinity of the Core-Forming Polyferrocene Block in the Micellar Morphologies Formed by Poly(ferrocenylsilane-*b*-dimethylsiloxane) in *n*-Alkane Solvents. *J. Am. Chem. Soc.* **2000**, *122* (47), 11577–11584.
- (11) Massey, J.; Power, K. N.; Manners, I.; Winnik, M. A. Self-Assembly of a Novel Organometallic–Inorganic Block Copolymer in Solution and the Solid State: Nonintrusive Observation of Novel Wormlike Poly(ferrocenyldimethylsilane)-*b*-Poly(dimethylsiloxane) Micelles. *J. Am. Chem. Soc.* **1998**, *120* (37), 9533–9540.
- (12) Cao, L.; Massey, J. A.; Winnik, M. A.; Manners, I.; Riethmüller, S.; Banhart, F.; Spatz, J. P.; Möller, M. Reactive Ion Etching of Cylindrical Polyferrocenylsilane Block Copolymer Micelles: Fabrication of Ceramic Nanolines on Semiconducting Substrates. *Adv. Funct. Mater.* **2003**, *13* (4), 271–276.
- (13) Jain, S.; Bates, F. S. Consequences of Nonergodicity in Aqueous Binary PEO–PB Micellar Dispersions. *Macromolecules* **2004**, *37* (4), 1511–1523.
- (14) Wang, X.; Guerin, G.; Wang, H.; Wang, Y.; Manners, I.; Winnik, M. A. Cylindrical Block Copolymer Micelles and Co-Micelles of Controlled Length and Architecture. *Science* **2007**, *317* (5838), 644–647.
- (15) Geng, Y.; Dalhaimer, P.; Cai, S.; Tsai, R.; Tewari, M.; Minko, T.; Discher, D. E. Shape effects of filaments versus spherical particles in flow and drug delivery. *Nat. Nanotechnol.* **2007**, *2* (4), 249–255.
- (16) Truong, N. P.; Quinn, J. F.; Anastasaki, A.; Haddleton, D. M.; Whittaker, M. R.; Davis, T. P. Facile access to thermoresponsive filomicelles with tuneable cores. *Chem. Commun.* **2016**, *52* (24), 4497–4500.
- (17) Oltra, N. S.; Swift, J.; Mahmud, A.; Rajagopal, K.; Loverde, S. M.; Discher, D. E. Filomicelles in nanomedicine - from flexible, fragmentable, and ligand-targetable drug carrier designs to combination therapy for brain tumors. *J. Mater. Chem. B* **2013**, *1* (39), 5177–5185.
- (18) Dalhaimer, P.; Engler, A. J.; Parthasarathy, R.; Discher, D. E. Targeted Worm Micelles. *Biomacromolecules* **2004**, *5* (5), 1714–1719.
- (19) Truong, N. P.; Quinn, J. F.; Whittaker, M. R.; Davis, T. P. Polymeric filomicelles and nanoworms: two decades of synthesis and application. *Polym. Chem.* **2016**, *7* (26), 4295–4312.
- (20) Won, Y.-Y.; Davis, H. T.; Bates, F. S. Giant Wormlike Rubber Micelles. *Science* **1999**, *283* (5404), 960–963.
- (21) Verber, R.; Blanazs, A.; Armes, S. P. Rheological studies of thermo-responsive diblock copolymer worm gels. *Soft Matter* **2012**, *8* (38), 9915–9922.
- (22) Geng, Y.; Discher, D. E. Visualization of degradable worm micelle breakdown in relation to drug release. *Polymer* **2006**, *47* (7), 2519–2525.
- (23) Geng, Y.; Discher, D. E. Hydrolytic Degradation of Poly(ethylene oxide)-*block*-Polycaprolactone Worm Micelles. *J. Am. Chem. Soc.* **2005**, *127* (37), 12780–12781.
- (24) Stigter, D. Intrinsic Viscosity and Flexibility of Rodlike Detergent Micelles. *J. Phys. Chem.* **1966**, *70* (4), 1323–1325.
- (25) Adams, D. J.; Topham, P. D. Peptide conjugate hydrogelators. *Soft Matter* **2010**, *6* (16), 3707–3721.
- (26) Yan, C.; Pochan, D. J. Rheological properties of peptide-based hydrogels for biomedical and other applications. *Chem. Soc. Rev.* **2010**, *39* (9), 3528–3540.
- (27) Zhou, M.; Smith, A. M.; Das, A. K.; Hodson, N. W.; Collins, R. F.; Ulijn, R. V.; Gough, J. E. Self-assembled peptide-based hydrogels as scaffolds for anchorage-dependent cells. *Biomaterials* **2009**, *30* (13), 2523–2530.
- (28) Fielding, L. A.; Lane, J. A.; Derry, M. J.; Mykhaylyk, O. O.; Armes, S. P. Thermo-responsive Diblock Copolymer Worm Gels in Non-polar Solvents. *J. Am. Chem. Soc.* **2014**, *136* (15), 5790–5798.
- (29) Tan, J.; Sun, H.; Yu, M.; Sumerlin, B. S.; Zhang, L. Photo-PISA: Shedding Light on Polymerization-Induced Self-Assembly. *ACS Macro Lett.* **2015**, *4* (11), 1249–1253.
- (30) Madsen, J.; Armes, S. P.; Bertal, K.; MacNeil, S.; Lewis, A. L. Preparation and Aqueous Solution Properties of Thermo-responsive Biocompatible AB Diblock Copolymers. *Biomacromolecules* **2009**, *10* (7), 1875–1887.
- (31) Doncom, K. E. B.; Warren, N. J.; Armes, S. P. Polysulfobetaine-based diblock copolymer nano-objects via polymerization-induced self-assembly. *Polym. Chem.* **2015**, *6* (41), 7264–7273.
- (32) Sun, Z.; Tian, Y.; Hom, W. L.; Gang, O.; Bhatia, S. R.; Grubbs, R. B. Translating Thermal Response of Triblock Copolymer Assemblies in Dilute Solution to Macroscopic Gelation and Phase Separation. *Angew. Chem., Int. Ed.* **2017**, *56* (6), 1491–1494.
- (33) Wanka, G.; Hoffmann, H.; Ulbricht, W. Phase Diagrams and Aggregation Behavior of Poly(oxyethylene)-Poly(oxypropylene)-Poly(oxyethylene) Triblock Copolymers in Aqueous Solutions. *Macromolecules* **1994**, *27* (15), 4145–4159.
- (34) Sawhney, A. S.; Pathak, C. P.; Hubbell, J. A. Bioerodible hydrogels based on photopolymerized poly(ethylene glycol)-co-

poly( $\alpha$ -hydroxy acid) diacrylate macromers. *Macromolecules* **1993**, *26* (4), 581–587.

(35) Obeng, M.; Milani, A. H.; Musa, M. S.; Cui, Z. X.; Fielding, L. A.; Farrand, L.; Goulding, M.; Saunders, B. R. Self-assembly of poly(lauryl methacrylate)-*b*-poly(benzyl methacrylate) nano-objects synthesised by ATRP and their temperature-responsive dispersion properties. *Soft Matter* **2017**, *13* (11), 2228–2238.

(36) Jain, S.; Bates, F. S. On the Origins of Morphological Complexity in Block Copolymer Surfactants. *Science* **2003**, *300* (5618), 460–464.

(37) Warren, N. J.; Armes, S. P. Polymerization-Induced Self-Assembly of Block Copolymer Nano-objects via RAFT Aqueous Dispersion Polymerization. *J. Am. Chem. Soc.* **2014**, *136* (29), 10174–10185.

(38) Canning, S. L.; Smith, G. N.; Armes, S. P. A Critical Appraisal of RAFT-Mediated Polymerization-Induced Self-Assembly. *Macromolecules* **2016**, *49* (6), 1985–2001.

(39) Derry, M. J.; Fielding, L. A.; Armes, S. P. Industrially-relevant polymerization-induced self-assembly formulations in non-polar solvents: RAFT dispersion polymerization of benzyl methacrylate. *Polym. Chem.* **2015**, *6* (16), 3054–3062.

(40) Cunningham, V. J.; Ratcliffe, L. P. D.; Blanazs, A.; Warren, N. J.; Smith, A. J.; Mykhaylyk, O. O.; Armes, S. P. Tuning the critical gelation temperature of thermo-responsive diblock copolymer worm gels. *Polym. Chem.* **2014**, *5* (21), 6307–6317.

(41) Warren, N. J.; Mykhaylyk, O. O.; Mahmood, D.; Ryan, A. J.; Armes, S. P. RAFT Aqueous Dispersion Polymerization Yields Poly(ethylene glycol)-Based Diblock Copolymer Nano-Objects with Predictable Single Phase Morphologies. *J. Am. Chem. Soc.* **2014**, *136* (3), 1023–1033.

(42) Sugihara, S.; Blanazs, A.; Armes, S. P.; Ryan, A. J.; Lewis, A. L. Aqueous Dispersion Polymerization: A New Paradigm for in Situ Block Copolymer Self-Assembly in Concentrated Solution. *J. Am. Chem. Soc.* **2011**, *133* (39), 15707–15713.

(43) Blanazs, A.; Ryan, A. J.; Armes, S. P. Predictive Phase Diagrams for RAFT Aqueous Dispersion Polymerization: Effect of Block Copolymer Composition, Molecular Weight, and Copolymer Concentration. *Macromolecules* **2012**, *45* (12), 5099–5107.

(44) Figg, C. A.; Carmean, R. N.; Bentz, K. C.; Mukherjee, S.; Savin, D. A.; Sumerlin, B. S. Tuning Hydrophobicity To Program Block Copolymer Assemblies from the Inside Out. *Macromolecules* **2017**, *50* (3), 935–943.

(45) Figg, C. A.; Simula, A.; Gebre, K. A.; Tucker, B. S.; Haddleton, D. M.; Sumerlin, B. S. Polymerization-induced thermal self-assembly (PITSA). *Chemical Science* **2015**, *6* (2), 1230–1236.

(46) Steinschulte, A. A.; Scotti, A.; Rahimi, K.; Nevskiy, O.; Oppermann, A.; Schneider, S.; Bochenek, S.; Schulte, M. F.; Geisel, K.; Jansen, F.; Jung, A.; Mallmann, S.; Winter, R.; Richtering, W.; Wöll, D.; Schweins, R.; Warren, N. J.; Plamper, F. A. Stimulated Transitions of Directed Nonequilibrium Self-Assemblies. *Adv. Mater.* **2017**, *29* (43), 1703495.

(47) Pei, Y.; Dharsana, N. C.; van Hensbergen, J. A.; Burford, R. P.; Roth, P. J.; Lowe, A. B. RAFT dispersion polymerization of 3-phenylpropyl methacrylate with poly[2-(dimethylamino)ethyl methacrylate] macro-CTAs in ethanol and associated thermoreversible polymorphism. *Soft Matter* **2014**, *10* (31), 5787–5796.

(48) Bauri, K.; Narayanan, A.; Haldar, U.; De, P. Polymerization-induced self-assembly driving chiral nanostructured materials. *Polym. Chem.* **2015**, *6* (34), 6152–6162.

(49) Semsarilar, M.; Jones, E. R.; Blanazs, A.; Armes, S. P. Efficient Synthesis of Sterically-Stabilized Nano-Objects via RAFT Dispersion Polymerization of Benzyl Methacrylate in Alcoholic Media. *Adv. Mater.* **2012**, *24* (25), 3378–3382.

(50) Zhang, X.; Boisson, F.; Colombani, O.; Chassenieux, C.; Charleux, B. Synthesis of Amphiphilic Poly(acrylic acid)-*b*-poly(*n*-butyl acrylate-co-acrylic acid) Block Copolymers with Various Microstructures via RAFT Polymerization in Water/Ethanol Heterogeneous Media. *Macromolecules* **2014**, *47* (1), 51–60.

(51) Ratcliffe, L. P. D.; McKenzie, B. E.; Le Bouëdec, G. M. D.; Williams, C. N.; Brown, S. L.; Armes, S. P. Polymerization-Induced Self-Assembly of All-Acrylic Diblock Copolymers via RAFT Dispersion Polymerization in Alkanes. *Macromolecules* **2015**, *48* (23), 8594–8607.

(52) Derry, M. J.; Fielding, L. A.; Warren, N. J.; Mable, C. J.; Smith, A. J.; Mykhaylyk, O. O.; Armes, S. P. In situ small-angle X-ray scattering studies of sterically-stabilized diblock copolymer nanoparticles formed during polymerization-induced self-assembly in non-polar media. *Chemical Science* **2016**, *7* (8), 5078–5090.

(53) Lovett, J. R.; Derry, M. J.; Yang, P.; Hatton, F. J.; Warren, N. J.; Fowler, P. W.; Armes, S. P. Can percolation theory explain the gelation behavior of diblock copolymer worms? *Chemical Science* **2018**, *9*, 7138–7144.

(54) Warren, N. J.; Rosselgong, J.; Madsen, J.; Armes, S. P. Disulfide-Functionalized Diblock Copolymer Worm Gels. *Biomacromolecules* **2015**, *16* (8), 2514–2521.

(55) Simon, K. A.; Warren, N. J.; Mosadegh, B.; Mohammady, M. R.; Whitesides, G. M.; Armes, S. P. Disulfide-Based Diblock Copolymer Worm Gels: A Wholly-Synthetic Thermoreversible 3D Matrix for Sheet-Based Cultures. *Biomacromolecules* **2015**, *16* (12), 3952–3958.

(56) Lovett, J. R.; Ratcliffe, L. P. D.; Warren, N. J.; Armes, S. P.; Smallridge, M. J.; Cracknell, R. B.; Saunders, B. R. A Robust Cross-Linking Strategy for Block Copolymer Worms Prepared via Polymerization-Induced Self-Assembly. *Macromolecules* **2016**, *49* (8), 2928–2941.

(57) Kocik, M. K.; Mykhaylyk, O. O.; Armes, S. P. Aqueous worm gels can be reconstituted from freeze-dried diblock copolymer powder. *Soft Matter* **2014**, *10* (22), 3984–3992.

(58) Canton, I.; Warren, N. J.; Chahal, A.; Amps, K.; Wood, A.; Weightman, R.; Wang, E.; Moore, H.; Armes, S. P. Mucin-Inspired Thermoresponsive Synthetic Hydrogels Induce Stasis in Human Pluripotent Stem Cells and Human Embryos. *ACS Cent. Sci.* **2016**, *2* (2), 65–74.

(59) Mitchell, D. E.; Lovett, J. R.; Armes, S. P.; Gibson, M. I. Combining Biomimetic Block Copolymer Worms with an Ice-Inhibiting Polymer for the Solvent-Free Cryopreservation of Red Blood Cells. *Angew. Chem., Int. Ed.* **2016**, *55* (8), 2801–2804.

(60) Ratcliffe, L. P. D.; Bentley, K. J.; Wehr, R.; Warren, N. J.; Saunders, B. R.; Armes, S. P. Cationic disulfide-functionalized worm gels. *Polym. Chem.* **2017**, *8* (38), 5962–5971.

(61) Mykhaylyk, O. O.; Warren, N. J.; Parnell, A. J.; Pfeifer, G.; Laeuger, J. Applications of shear-induced polarized light imaging (SIPLI) technique for mechano-optical rheology of polymers and soft matter materials. *J. Polym. Sci., Part B: Polym. Phys.* **2016**, *54* (21), 2151–2170.

(62) Mykhaylyk, O. O.; Parnell, A. J.; Pryke, A.; Fairclough, J. P. A. Direct Imaging of the Orientational Dynamics of Block Copolymer Lamellar Phase Subjected to Shear Flow. *Macromolecules* **2012**, *45* (12), 5260–5272.

(63) Holland, C.; Vollrath, F.; Ryan, A. J.; Mykhaylyk, O. O. Silk and Synthetic Polymers: Reconciling 100 Degrees of Separation. *Adv. Mater.* **2012**, *24* (1), 105–109.

(64) Blanazs, A.; Madsen, J.; Battaglia, G.; Ryan, A. J.; Armes, S. P. Mechanistic Insights for Block Copolymer Morphologies: How Do Worms Form Vesicles? *J. Am. Chem. Soc.* **2011**, *133* (41), 16581–16587.

(65) Ilavsky, J.; Jemian, P. R. Irena: tool suite for modeling and analysis of small-angle scattering. *J. Appl. Crystallogr.* **2009**, *42*, 347–353.

(66) Warren, N. J.; Mykhaylyk, O. O.; Ryan, A. J.; Williams, M.; Doussineau, T.; Dugourd, P.; Antoine, R.; Portale, G.; Armes, S. P. Testing the vesicular morphology to destruction: birth and death of diblock copolymer vesicles prepared via polymerization-induced self-assembly. *J. Am. Chem. Soc.* **2015**, *137* (5), 1929–37.

(67) Mable, C. J.; Thompson, K. L.; Derry, M. J.; Mykhaylyk, O. O.; Binks, B. P.; Armes, S. P. ABC Triblock Copolymer Worms: Synthesis, Characterization, and Evaluation as Pickering Emulsifiers

for Millimeter-Sized Droplets. *Macromolecules* **2016**, *49* (20), 7897–7907.

(68) LaRue, I.; Adam, M.; Pitsikalis, M.; Hadjichristidis, N.; Rubinstein, M.; Sheiko, S. S. Reversible Morphological Transitions of Polystyrene-*b*-polyisoprene Micelles. *Macromolecules* **2006**, *39* (1), 309–314.

(69) Sundararaman, A.; Stephan, T.; Grubbs, R. B. Reversible Restructuring of Aqueous Block Copolymer Assemblies through Stimulus-Induced Changes in Amphiphilicity. *J. Am. Chem. Soc.* **2008**, *130* (37), 12264–12265.

(70) Moughton, A. O.; O'Reilly, R. K. Thermally induced micelle to vesicle morphology transition for a charged chain end diblock copolymer. *Chem. Commun.* **2010**, *46* (7), 1091–1093.

(71) Cai, Y.; Aubrecht, K. B.; Grubbs, R. B. Thermally Induced Changes in Amphiphilicity Drive Reversible Restructuring of Assemblies of ABC Triblock Copolymers with Statistical Polyether Blocks. *J. Am. Chem. Soc.* **2011**, *133* (4), 1058–1065.

(72) Lovett, J. R.; Warren, N. J.; Armes, S. P.; Smallridge, M. J.; Cracknell, R. B. Order–Order Morphological Transitions for Dual Stimulus Responsive Diblock Copolymer Vesicles. *Macromolecules* **2016**, *49* (3), 1016–1025.

(73) Deng, R.; Derry, M. J.; Mable, C. J.; Ning, Y.; Armes, S. P. Using Dynamic Covalent Chemistry To Drive Morphological Transitions: Controlled Release of Encapsulated Nanoparticles from Block Copolymer Vesicles. *J. Am. Chem. Soc.* **2017**, *139* (22), 7616–7623.

(74) Penfold, N. J. W.; Lovett, J. R.; Warren, N. J.; Verstraete, P.; Smets, J.; Armes, S. P. pH-Responsive non-ionic diblock copolymers: protonation of a morpholine end-group induces an order-order transition. *Polym. Chem.* **2016**, *7* (1), 79–88.

(75) Barnes, H. A. A. *Handbook of Elementary Rheology*; The University of Wales Institute of Non-Newtonian Fluid Mechanics: Aberystwyth, 2000.

(76) Spenley, N. A.; Cates, M. E.; McLeish, T. C. B. Nonlinear rheology of wormlike micelles. *Phys. Rev. Lett.* **1993**, *71* (6), 939–942.

(77) Glatter, O.; Kratky, O. *Small-Angle X-ray Scattering*; Academic Press: London, 1982.

(78) Raghavan, S. R.; Douglas, J. F. The conundrum of gel formation by molecular nanofibers, wormlike micelles, and filamentous proteins: gelation without cross-links? *Soft Matter* **2012**, *8* (33), 8539–8546.

(79) Alexandridis, P.; Holzwarth, J. F.; Hatton, T. A. Micellization of Poly(ethylene oxide)-Poly(propylene oxide)-Poly(ethylene oxide) Triblock Copolymers in Aqueous Solutions: Thermodynamics of Copolymer Association. *Macromolecules* **1994**, *27* (9), 2414–2425.

(80) Vogtt, K.; Beaucage, G.; Weaver, M.; Jiang, H. Scattering Function for Branched Wormlike Chains. *Langmuir* **2015**, *31* (30), 8228–8234.